Dynamic Microstructured Thermoresponsive Interfaces for Label-Free Cell Sorting Based on Nonspecific Interactions

Ronaldo Badenhorst[a], Sergei V. Makaev[a], Mikhail Parker[a#], Rostyslav Marunych[b#], Vladimir Reukov[c], Agnieszka Będzińska[b], Olexandr Korchynskyi[b], Ostap Kalyuzhnyi[d], Dmytro Yaremchuk[d,e], Jaroslav Ilnytskyi [d,e], Taras Patsahan[d,e], Sergiy Minko[a]*

[a] Nanostructured Materials Lab, University of Georgia, Athens, 30602 GA, United States

[b] Laboratory of Experimental Biology and Department of Biochemistry & General Chemistry, Medical Faculty, Rzeszów University; Warzywna 1a Str., 35-959, Rzeszów, Poland

[c] Regenerative Bioscience Center, Department of Textiles, Merchandising and Interiors, Athens, 30602 GA, United States

[d] Institute for Condensed Matter Physics of the National Academy of Sciences of Ukraine, 1 Svientsitskii str., 79011, Lviv, Ukraine

[e] Institute of Applied Mathematics and Fundamental Sciences, Lviv Polytechnic National University, 12 S. Bandera Str., 79013, Lviv, Ukraine

[#] equal contribution

ABSTRACT

Label-free cell-sorting methods and materials are developed in this work. The microstructured thermoresponsive surfaces made of poly (glycidyl methacrylate) (PGMA) and poly(N-isopropylacrylamide-co-glycidyl methacrylate) (PNIPAM-co-GMA) are prepared by phase separation on the submicron scale in thin films, then crosslinked and covalently grafted to the substrate. PGMA domains are used for cell adhesion, while the PNIPAM-co-GMA matrix pushes cells off the surface at a temperature below the lower critical solution temperature (LCST). The microstructure formation and swelling-shrinking caused by changes in temperature are studied experimentally and using dissipative particle dynamics computer simulations. Experiments with RAW 264.7 murine macrophage-like cells, NIH3T3/GFP murine fibroblasts, and HaCaT human skin keratinocytes (unlabeled and GFP-positive strains) demonstrate successful cell sorting based on the weak and nonspecific interactions with the reconfigurable thermoresponsive microstructured surfaces. Efficient sorting with a separation factor above 50 is achieved if the push-off force is adjusted to the level between the adhesive forces of the separating cells. This experimental finding is supported by the Monte Carlo simulations of cell adsorption and detachment on the microstructured surfaces. The experiment and simulations show that efficient cell sorting is possible for weak to moderate cell adhesion to the surfaces. However, the method

is not successful for very weak and very strong adhesion. We demonstrate that the cell adhesion to the microstructured surfaces can be adjusted by changes in conditions of the phase separation at the stage of the film formation and variation of the incubation time of the cells on the microstructured surfaces.

KEYWORDS: label-free cell sorting, reconfigurable microstructured surface, cell adhesion, phase separation in thin films, DPD simulations, Monte Carlo simulations

1. INTRODUCTION

Discrimination of cells and non-cellular life forms (LF), such as viruses, in natural or artificial cell mixtures in their environment is crucial across various fields of biology, medicine, and biotechnology. Cell sorting methods are based on differences in the composition of cell membranes and on the physical properties of cells. All cell sorting methods can be divided into two groups: label-based and label-free. Fluorescence-activated LF sorting[1] (FACS) is commonly regarded as a major gold standard label-based method. This technology relies on the exclusive specificity of antibodies generated against different epitopes of cell surface markers. Unique fragments of polypeptides, carbohydrates, lipids, or other modifications within cell-type-specific surface proteins serve as convenient antibody targets. Therefore, isolation of the specific cell type from complex multicomponent mixes of different cells, like circulating blood cellular components, requires expensive equipment and extensive sets of costly antibodies. An alternative antibody-based technique, magnetic-activated cell sorting (magnetic beads conjugated with antibodies),[2] (MACS) does not require expensive equipment and is less time-consuming but is similarly dependent on costly antibodies. Unfortunately, all existing cell sorting procedures also generate a significant risk for mechanical cell damage and loss (around 7-14% for MACS procedure and up to 70% in the case of FACS process[3]). In addition, many convenient surface protein targets represent signaling molecules. Highly specific protein-protein interactions of antibodies with such surface targets simultaneously generate a risk of corresponding signaling pathway activation.

Alternative label-free methods explore differences in cell size,[4] electrical charges,[5] isoelectric points in an aqueous environment,[6] and mechanical properties.[7] Cell sorting based on cell density variations uses the density gradient centrifugation method.[8] Among other label-free methods, microfluidic methods have gained significant interest.[9-10] Microfluidic devices are classified into passive and active methods.[11] Passive methods use flow and geometry for cell sorting, while active methods, such as magnetophoresis, acoustophoresis, and dielectrophoresis, refer to cell response to applied external fields. However, quite often, the differences in the mentioned cell

properties are not significant between different cells, and it is virtually impossible to use these approaches as universal label-free sorting methods.

Adhesion-based sorting methods have attracted special attention for cell sorting because of the potential scalability and simplicity of the methods, similar to chromatography, which is broadly applied for separating small molecules. Several approaches were used and tested for the cell affinity-based sorting. One of the approaches is to decorate the adsorbent surface or components of microfluidic devices with antibodies.[12-13] In the latter case, cell sorting is based on the differences in specific and nonspecific interactions. Generally, this approach is very similar conceptually to MACS label-based sorting. Because of the competition between specific and nonspecific interactions, the efficiency of cell sorting will strongly depend on the cell mixture and overall cell concentrations. For highly asymmetric mixtures, when the cell of interest is a minority fraction, nonspecifically bound cells can occupy and block access to antibodies. Nonspecifically bound cells can be detached by the liquid flow. However, its efficiency depends on the flow uniformity along the adsorbent surface and the surface concentration of the bound cells. The experimental studies reported the efficiency of catching target cells from 30%[12] to 100%.[13] The impact of nonspecific adsorption can be minimized by using microstructured surfaces (typically an array of micropillars).[14] In the latter case, the contact surface area of the cell-microstructured surface is minimal, making it easier to adjust the liquid flow threshold to remove nonspecifically bound cells. However, most of these methods are non-continuous and non-scalable separations, which implies limitations for many applications.

Using weaker adherent-specific motifs (moderately selective motifs) helped to realize a continuous cell sorting method.[15-18] In one of the examples, the target cells are periodically attracted in the flow by adhesive patterns, roll over the pattern, released at the edge of the adhesive and non-adhesive pattern, and attracted again by the next adhesive pattern so that the suspended waste is removed with a flow into a side channel while target cells reside close to the microstructured surfaces and extracted from the main channel. For example, a purity of 92% was achieved in 30 min for the separation of neutrophils from blood.[15]

Another less-explored approach to adhesion-based sorting relies on differences in nonspecific cell interactions.[19] The essential advantage is that there is no need to use expensive antibodies or other types of selective ligands. However, this method is sensitive to cell-binding kinetics, which involves many biological aspects. Cell medium, extracellular matrix (ECM) proteins, and proteins secreted by cells can bind to the adsorbent surface and establish specific interactions via the integrin complex and focal adhesion formation.[20] For example, such an approach was used to

separate adherent and non-adherent cells[21] while aiming to separate pseudonormal breast epithelial cells (MCF10A) and cancer cells (MCF7).[19] It was found that the adhesion level plateaus for many cells after 1-2 h of cell incubation. For many applications, one round of cell sorting in such non-continuous methods is insufficient for highly asymmetric cell mixtures. Multiple cycles for 1-2h steps can take many days to reach a high separation level. A reasonable separation time was reported by Green and Murthy[22] about a nonspecific peptide-decorated flow setup to achieve 90% separation and removal of undesired cells, with a 45% loss of desired cells in a 3-stage 1.5 h process while maintaining cell viability post-separation.

The immensely successful developments of label-free methods provide various technical solutions for efficient cell sorting using microfluidic devices and micropatterned surfaces with highly- and moderately selective motifs in periodic and continuous flow processes. An obvious advantage of the application of moderately selective motifs is continuous technology. The drawback is the complex design of microfluidic devices and limited possibilities for scale-up. The question of the potential of nonspecific adhesion-based label-free scalable sorting remains intriguing because of the limited literature.

There are at least two basic problems to be solved. In contrast to antibody-based cell sorting, sorting and separating affinity-based small molecules involve the adsorption-desorption equilibrium at the adsorbent surface. This method is efficient and inexpensive at different scales, from lab analysis to industrial adsorption columns (column contact adsorbers). However, this method cannot be applied to cells because of the high contact surface area of the cell with the adsorbent. The latter is manifested in a very slow desorption process at the cell culture temperature.[23-25] The adsorption energy of small molecules scales with a few kT, while the cell-adsorbent energy can approach hundreds to thousands kT (where kT provides the energy scale of thermal fluctuations).[26] The affinity-based adsorption equilibrium based on thermal fluctuations cannot be established for cells. An affinity-based sorting of cells could be achieved by overcoming the high desorption energy barrier using external energy sources, such as shear flow,[27] ultrasound[28-29], or microfluidic devices discussed above. A precise and uniform adjustment of detachment forces using shear forces of a liquid flux or ultrasound sources is difficult to achieve at large scales.

The second problem is related to cell biology, which is specifically important for adherent cells. Cell-surface interactions are kinetically subdivided into phases. The first phase is Van der Waals forces, hydrogen bonds, hydrophobic, and ionic forces,[30-31] in the range of seconds. It is closely followed by the second phase of integrin protein association with ligands in the cellular

surroundings and binding to the surface exposed to cellular media containing proteins.[32-33] Further eventual interactions involve phase three of cell flattening and surface spreading through cellular receptor clustering and cytoskeletal reconstruction. Finally, after 24 h, cells secrete ECM, proliferate, and form tissue[34-35]. Adherent cells survive in suspension for a short time. They grow on adhesive surfaces (typically amphiphilic). The most common method to harvest them is to use proteases to cut the protein complex connection to the surface. The “shaved” cells can then be transferred to another container with media, where they can synthesize the membrane proteins and bind to the surface. The only short window for nonspecific interaction-based sorting of these cells is immediately after harvesting. In this case, biological processes do not likely interfere, and the cell can be considered as a patchy elastic colloidal particle. However, the composition of the membrane molecules will depend on the harvesting method. Another biological aspect of concern is cell viability and turning on “wrong” signaling after sorting. Regarding this aspect, a weak adhesive interaction of cells with the substrate could be beneficial.

Recently, we reported one step in the direction of affinity-based cell sorting using microstructured surfaces composed of cell-binding microdomains and thermoresponsive domains that undergo shrink-swell transition at the lower critical solution temperature (LCST).[36] Our concept refers to replacing the shear force of a liquid flux with an osmotic pushing-off force for cell detachment, assuming that this design is beneficial for uniform generation of cell detachment force for high volumes of cell sorting and manufacturing. The thermoresponsive domains were made of tethered poly(N-isopropylacrylamide) (PNIPAM), which changes its interaction with the aqueous environment and undergoes phase transition with temperature changes.[37] The reversible phase transition in the thermoresponsive system was introduced by the change of temperature around the LCST (32 °C for PNIPAM). The phase transition resulted in a reversible swelling/shrinking of the thermoresponsive domains. The latter process developed a push-off force to cause cell detachment. During the cold phase (30 °C), the cells were pushed off; during the warm phase (37 °C), the cells adsorbed on the surface. The affinity-based sorting was established when stronger bound cells stayed on the surface. At the same time, weakly bound cells were pushed off the surface and resided in the solution. The binding domains contained RGD (arginyl-glycyl-aspartic acid) cell-adhesive motifs. That helped us to discriminate cells with overexpressed integrin (cancer cells) from highly asymmetric mixtures with healthy cells. Importantly, the microstructured surface was designed appropriately to reach only the detachment of the cells that weakly interact with the surface and not to detach all cells that can be used for cell harvesting applications.[38] In the previous work, we used RGD affinity motifs bound to the adhesive domains.[36]

The following step to the LF nonspecific sorting was to model cell interaction with the microstructured dynamic surface using colloidal particles of a spherical or disk-like shape. We analyzed the effect of geometry and dimensions of the microstructured domains to approach the LCST-induced swelling of PNIPAM domains sufficient to weaken particle binding to the surface and push the particles off the surface in a controlled way.[39-40]

Here, we report on the next step for the LF sorting by avoiding selective motifs to demonstrate the feasibility of sorting based on nonspecific cell adsorption on the microstructured surfaces. In this case, the binding domains are made of crosslinked poly(glycidyl methacrylate) (PGMA), and thermoresponsive domains are made of a crosslinked copolymer of PNIPAM and PGMA (PNIPAM-co-PGMA). PGMA is an amphiphilic polymer with a hydrophobic backbone and hydrophilic –OH side functional groups formed after the opening of the epoxy ring. We show that different types of mammalian cells can be sorted on this surface owing to differences in the interaction of the cells with PGMA domains. To verify the label-free sorting, we used specially labeled cells with recombinant proteins. The invention of jellyfish *Aequorea victoria* green fluorescent protein (GFP) with its derivatives and mFruit seria of similar proteins generated a true revolution in live cell and tissue imaging.[41] Different colored versions of the modified fluorescent proteins span the whole range of visible light. Such a wide spectrum allows us to identify and discriminate specifically labeled cells, proteins, or even tissues within a whole recombinant organism.[42] Generation of recombinant proteins fused to parts of GFP allows the study of protein-protein interactions in live cells.[43] Alternatively, the fluorescent proteins labeled cells can be sorted with a conventional flow cytometric sorting without the involvement of expensive antibodies. Therefore, fluorescent proteins became very convenient for the visualization and quantification of reporter genes.

The ultimate goal of this work is to develop a scalable method of cell harvesting and sorting using cost-efficient cell sorting technology and materials. In this work, we demonstrate that lithography for the microstructured surfaces can be replaced by a more cost-efficient microphase separation method.

2. EXPERIMENTAL PART AND COMPUTER MODELING

2.1. Materials. Silicon wafers (Si-wafers) were purchased from University Wafer, Boston, MA, USA. (3-Glycidyloxypropyl)trimethoxysilane (GOPTMS), *N*-isopropylacrylamide (NIPAM), glycidyl methacrylate (GMA), azobisisobutyronitrile (AIBN) were purchased from Millipore-Sigma, USA; 1,4-dioxane was purchased from Lab Alley, USA; toluene, methyl ethyl ketone (MEK), hexane and ethanol were purchased from VWR Chemicals, USA; hydrogen peroxide (H_2O_2), and

ammonium hydroxide (NH_4OH) were purchased from Fischer Scientific, USA. Deionized (DI) water was prepared in the lab using ion-exchange filters supplied by Evoqua, USA. Linear polyethyleneimine (PEI), MW=25 kg/mol was purchased from Polysciences Inc., Warrington, PA, USA. Lentiviral construct encoding enhanced GFP, (eGFP) was kindly provided by Dr. Antoine A.F. de Vries, Leiden University Medical Center, Leiden, The Netherlands.

2.2. Synthesis of polymers. PGMA and PNIPAM-co-GMA were synthesized in the lab as described below. PGMA homopolymer was synthesized using solution radical polymerization. GMA was dissolved in MEK (25 wt.% monomer solution) and purified on an inhibitor removal column. AIBN was added to the solution for a 0.3 M concentration in the reaction mixture. The solution was purged with argon for 15 minutes; the polymerization was conducted for 2 h in a water bath at 40 °C and stopped by opening the cap, after which the polymer was precipitated 5 times from MEK in ethanol. The polymer yield was 50%. Mw=570 kg/mol. M_w/M_n=3.0 (gel-permeation chromatography data, GPC, chloroform).

A random copolymer PNIPAM-co-GMA was synthesized using solution radical polymerization. Recrystallized from hexane and purified on an aluminum oxide column NIPAM and GMA purified on an inhibitor removal aluminum oxide column, were dissolved in MEK at a ratio NIPAM:GMA=95:5 to prepare a 40 wt.% monomer solution. AIBN was added to the solution for a 0.08 M concentration in the reaction mixture. The solution was purged with argon for 15 minutes; the polymerization was conducted for 2 h in a water bath at 40 °C and stopped by opening the cap, after which the copolymer was precipitated 5 times from MEK in hexane. The polymer yield was 80%. Mw=250 kg/mol M_w/M_n=2.01 (GPC, chloroform). NIPAM:GMA ratio in the resulting copolymer was calculated by integrating intensities of amide groups from NIPAM and ester groups from GMA on FTIR spectra (Figure S1). (PerkinElmer Frontier); for 95:5 mole ratio of the feed solution, the calculated molar content of GMA was 5.3%.

Poly(*N*-isopropylacrylamide) (PNIPAM) was synthesized similarly to PNIPAM-co-GMA copolymer, without adding GMA. The polymer yield was 40%. M_w =120 kg/mol M_w/M_n= 2.0 (GPC, chloroform).

The phase behavior of PNIPAM-co-GMA aqueous solutions was tested using turbidimetry (Figure S2). In contrast to PNIPAM homopolymer solutions with LCST= 32.5 °C, the PNIPAM-co-GMA copolymer (GMA 5.3% mol) has LCST=28.5 °C.

The thermal characteristics of the bulk polymers (differential scanning calorimetry, DSC) reveal typical glass transition temperatures for crosslinked PGMA and PNIPAM 60 °C and 135 °C,

respectively (Figures S3, S4 and S5). The crosslinked PNIPAM-co-GMA copolymer and homopolymer PNIPAM DSC plots are identical.

2.3. Cell cultures and media. Cell cultures: NIH3T3/GFP murine fibroblasts (further referenced as 3T3) have been generously donated by BioAesthetic, Durham, NC. These cells stably express gene-reporter for Green Fluorescent Protein (GFP) for detection and identification. RAW 264.7 murine macrophage-like cells (further referenced as RAW) were purchased from ATCC, USA. Human skin keratinocytes of HaCaT cell line and HEK293T cells were kindly provided by Prof. Peter ten Dijke, Leiden University Medical Center, Leiden, Netherlands. Dulbecco's modified Eagle's medium (DMEM) (Cat. No. D6429), Fetal Bovine Serum (FBS) (Cat. No. ES-009-B), L-glutamine (Cat. No. TMS-002-C), sodium pyruvate (Cat. No. TMS-005-B), β-mercaptoethanol (Cat. No. ES-007-E), Antibiotic-Antimycotic (Cat. No. 15-240-112), trypsin-EDTA (Cat. No. T4049), Dulbecco's Phosphate Buffered Saline (DPBS) (Cat. No. D8537), were purchased from Millipore-Sigma, USA.

2.4. Amplification of lentiviral particles and lentiviral transduction of cells. All the procedures of lentivirus particle amplification and infection were performed at BSL2 lab facility. VSV-G pseudotyped lentiviral particles were amplified in HEK293T cells. Briefly, HEK23T cells at 60% confluency were transfected with a mixture of four plasmids: 1. Lentiviral construct; 2, VSV-G; 3. HIV-GAG/Pol and 4. pRSV-Rev at a molar ratio 2:1:1:1 using PEI. 46 hours upon transfection, supernatant from virus-producing cells was collected, cleared from cell debris by centrifugation at 6,000g, aliquoted, and frozen at 80 °C. A freshly thawed aliquot of lentiviral particles was added to model cells cultured in their complete growth medium supplemented with 10 μg/ml of DEAE dextran for 8 hours. 48 hours after transduction, the efficiently infected cells were selected with 1 μg/ml of puromycin for three to five days. After five days, culture supernatant was collected for ELISA control specific for p24 HIV envelope protein, and if negative, cells were transferred to BSL1 lab and used in the study.

2.5. Fabrication of microstructured thermoresponsive coatings. *Functionalization of the surface of Si-wafers*. After cutting Si-wafers into 1 x 1 cm^2 square samples, they were cleaned in piranha solution (1:1:1 ratio of ammonium hydroxide, DI water, and H_2O_2) for 60 min at 70 °C. The cleaned samples were rinsed with DI water and ethanol and dried under an argon flux. After washing and cleaning the Si-wafers, they were immersed in a 1 % GOPTMS solution in toluene for 10 h to functionalize the surface with epoxy groups for further use.

Step 1. Fabrication of PGMA microdomains. Solution of three different (1:5, 1:10 & 1:18) ratios of 5% w/w PGMA and 4% w/w PNIPAM were prepared in dioxane. The solution was deposited on

the GOPTMS-treated Si-wafers using spin-coating at 7000 RPM for 30 s. Following the deposition, the sample was placed on a 150 °C heating plate for 3 min to ensure PGMA partial crosslinking (Figure S6).

Step 2. Fabrication of the microstructured coatings. The sample prepared in Step 1 was rinsed in DI water for 15 min to dissolve the PNIPAM matrix and dried under argon flux. Two different 1% and 2% w/w PNIPAM-co-GMA solutions in ethanol were used to spin-coat over the PGMA domain-decorated Si-wafers at 7000 RPM. Following the deposition, the samples were placed in a vacuum oven at 185 °C for 2 h to ensure crosslinking of PNIPAM-co-GMA and grafting it to the GOPTMS surface (Figure S7). The fabricated samples consisted of dual (PGMA and PNIPAM-co-GMA) domains and were fabricated using the ratios as follows: 1:5/1%, 1:5/2%, 1:10/1%, 1:10/2%, 1:18/1%, 1:18/2%, which explains the ratios of PGMA and PNIPAM for the deposition of PGMA domains (in the nominator) and the concentration of PNIPAM-co-GMA for the deposition of PNIPAM-co-GMA domains (in the denominator). The surfaces used for later testing will be referred to as A1, A2, B1, B2, C1, and C2, with A 1:5, B 1:10, and C 1:18 PGMA:PNIPAM solutions ratios, while 1 and 2 annotations refer to PNIPAM-co-PGMA solution concentrations. As a control, PGMA and PNIPAM-co-GMA uniform single-component films were fabricated.

Plasma etching of microstructured dual domain. The excess of PNIPAM-co-GMA over PGMA domains was removed using vacuum plasma etching for 1 min with Harrick Plasma PDC-001 at max power (~30 W, 0.8 mm Hg air) (Figure S8). The etched PNIPAM-co-GMA thickness was determined from the analysis of SPM images before and after PNIPAM-co-GMA deposition. The etching time was adjusted based on the etching kinetics (Figure S9).

2.6. Characterization of the microstructured surface: simulations. Understanding the details of the structure of the microstructured surfaces obtained in Step 1 was targeted using the dissipative particle dynamics (DPD) method[44], which allows for reaching the mesoscale while retaining principal chemical features on a coarse-grained level. The repeating units of PGMA and PNIPAM chains are treated as a single soft bead of roughly 10 atoms. Explicit water is modeled as a set of separate beads. Such model chains were given the possibility to both phase separate and to be grafted to the substrate. Details of the parametrization of the model can be found in SI.

Swelling of PNIPAM-co-GMA matrix was simulated when considering grafting to the crosslinked network to the substrate (GOPTMS-treated basal surface of Si-wafer in the experiments) and to PGMA domains that carry unreacted yet epoxy-functional groups. The computer simulations applying DPD method were used to analyze the potential effect of additional pinning of the matrix by PGMA domains. Details of the model can be found in SI.

2.7. Characterization of the microstructured surfaces: experiments. The samples of the microstructured surfaces were analyzed using scanning probe microscopy (SPM) with Dimension Icon and MultiMode 8 (Bruker) microscopes. The sample characterization was performed for the dry samples in air and in water at room temperature and at 40 °C. The scanning conditions in air: 10x10 to 40x40 μm scan with resolution 256x256 and 1024x1024 pixels in PeakForce Air mode with TESP probe (spring constant ~40 N/m); in water: 10x10 to 20x20 μm scan with resolution 256x256 and 512x512 pixels in PeakForce Fluid mode with PNP-TR-Au probe (spring constant ~0.08 N/m). The same sample was scanned at least four times: 1) after spin-coating, short-time annealing, and washing out PNIPAM, assuming that short-time annealing (150 °C, 3 min) does not affect the structure of the PNIPAM domains; we consider that these SPM scans reflect the structure of PGMA domains formed in the phase separation stage; 2) after deposition of PNIPAM-co-GMA and long-time annealing (185 °C, 2 h), assuming that the structure are initially changes and then crosslinked; 3) after plasma treatment; and 4) in water above and below LCST. Not all samples were scanned in water at T>LCST, because we observed no substantial differences between samples scanned in air and water at T>LCST.

2.8 Cell-sorting experiments. *Establishing the strength of cell attachment after 20 min (short) incubation (cells used in the experiments: RAW, 3T3, HaCaT).* Approximately 20000 cells per 100 μl droplet of 37 °C DMEM were deposited on the preheated at 37 °C microstructure-coated Si-wafers that were glued to the bottom of the Petri dish. The droplet was placed directly on top of the wafer. Following the deposition, the samples were incubated in a CO_2 incubator at 37 °C for 20 min to let all cells settle down on the surfaces. Then, the wafer was immediately placed under the optical microscope (Olympus BX-51 microscope equipped with Tucsen TCC-3.3ICE-N camera under 5x magnification). Images were recorded under brightfield illumination and green fluorescent illumination. After collection of images of the attached cells in several locations (up to 7 for each wafer), the samples were washed with 2 ml of ice-cold PBS by pipetting and pictured under the microscope to determine the degree of cell detachment. The experiment was repeated with a flow-through system (Figure S10) using a peristaltic pump instead of pipetting, where the strength of the flow shear force could be estimated. PGMA-only and PNIPAM-only surfaces were used as controls. NOTE: Since seeding timing was of high importance – cells were seeded not simultaneously but one wafer at a time.

Establishing the strength of cell attachment after 16 h (long) incubation for the cells RAW, 3T3, HaCaT. For the overnight attachment study, cells were seeded on the microdomain-coated Si-wafers. The wafers were glued in a well of a 6-well plate. Aapproximately 40000 cells in 4 ml of

37 °C DMEM media were seeded. After that, the plates were incubated overnight (approx. 16 hours) in the CO_2 incubator at 37 °C. The next day, Si-wafers were pictured under the microscope, washed with ice-cold PBS by pipetting and in the flow-through system, and pictured again to determine the degree of cell detachment. NOTE: Since the change of temperature might have affected cell detachment, wafers were investigated not simultaneously but one by one.

Mixed cells sorting after 20 min (short) incubation. The short incubation time protocol was repeated for mixtures of 3T3/RAW, 3T3/HaCaT and HaCaT/RAW cells, which had about 20000 cells of each cell type (40000 total).

Mixed cells sorting after 1 h (median) incubation. Since HaCaT cells require a longer time to properly attach to PGMA surfaces, the sorting experiment was repeated for 3T3/HaCaT and HaCaT/RAW cell mixture with 1 h incubation time.

Mixed cells sorting after 16 h (long) incubation. The long incubation time protocol was repeated for a mixture of 3T3/RAW, 3T3/HaCaT, and HaCaT/RAW cells. For the initial 3T3/RAW mixed seeding, we used 20000 3T3 and 10000 RAW cells (30000 total). For HaCaT/RAW, 20000 HaCaT and 10000 RAW cells were also used (30000 total). And for 3T3/HaCaT, 15000 cells of each were used in the experiment. This ratio was selected taking into account that the average doubling time of RAW cells is about 15 hours, while 3T3 and HaCaT, 18-26 hours and 26-28 hours, respectively.

Image analysis. Images of the seeded cell cultures were analyzed by counting cells on the microstructured and control surfaces using ImageJ software, typically by thresholding the pictures after applying several filters (background subtraction, blurring, and segmentation). Brightfield pictures were used to count the total number of cells. GFP-modified cells fluoresce under blue light, emitting green light. Therefore, green fluorescent pictures were used to count only GFP-modified cells. The count of non-fluorescent cells was obtained from the subtraction of GFP-modified cell counts from the total number of cells.

2.9. Monte Carlo simulations of cell sorting. Adhesive domains of the microstructured surface were modeled as an array of cylindrical objects aligned in a plane along the surface, with their axes oriented orthogonally to it. All domains are assumed to have equal dimensions (both height and diameter) and are randomly distributed over the surface without overlap. Positions and orientations of the domains are fixed throughout the simulation. The top domain surfaces exhibit adhesive interactions with the cell surface, and the adhesion energy depends linearly on the contact area between the cell and the domain surfaces. The space between domains along the

surface is filled with a polymer phase. In the collapsed state, the polymers do not interact with the cell. In the swollen state, the polymer phase rises above the domain level and repels the cell from the surface. The cell is modeled as spherical particles while suspended in solution, but it may also deform upon contact with the surface, increasing its contact area at the cell-domain interface. The contact period is assumed to be short enough that the cell's overall shape and dimensions remain unchanged. The local deformation at the interface between the cell and domains is represented as a flat circular intersection of the cell sphere, with the diameter of this section determined by the distance between the cell center and the cell-domain interface. The extent of deformation is limited by the minimum available distance between the cell center and the cell-domain interface. Since a cell can simultaneously contact multiple domains, the attractive interaction between the cell and the surface results from the sum of interactions between the cell and all domains in contact. The cell can immerse into the swollen polymer phase until it is stopped by contact with a domain surface and by reaching its maximum extent of deformation. The energy of repulsive interaction is determined by the circular intersection between the cell sphere and the polymer phase surface, which is located above the domain surface. The intersection between the cell sphere and the polymer phase should exclude regions occupied by the domains, regardless of how much higher the polymer phase surface is compared to the domain surfaces. The cells interact with each other as hard spheres. In addition to the attractive and repulsive interactions, there is also a hard-wall interaction between the cells and the surface domains. Since all gaps between the domains are smaller than the cell size, the cell cannot penetrate below the level of the domain's top surface. Due to being denser than the surrounding solution, the cells precipitate onto the patterned surface under gravity. The model incorporates gravity as an external field that drives the cells toward the microstructured surface, with the associated interaction energy varying linearly with the distance between the cell centers and the surface. Cells exhibit random motion resulting from disturbances induced by intrinsic sources (e.g., fluid flow, shear gradients, hydrodynamic instabilities, substrate vibration). These sources are non-thermal, but in terms of our simulation, they play the same role as fluctuation noise produced by the temperature. At the same time, real thermal fluctuations are considered negligibly small for such large objects as cells. Details of the model and methods are discussed in SI.

3. RESULTS AND DISCUSSIONS

3.1. General concept. The concept of cell sorting using microstructured thermoresponsive surfaces or coatings is illustrated in Figure 1. The coating is constituted of two different

microdomains. One domain type (made of PGMA) is adhesive to cells (nonspecific weak adhesion), while the second domain type is a matrix made of PNIPAM-co-GMA, which pushes off the cells from the surface upon swelling at a temperature below the LCST. Importantly, efficient cell detachment can be approached if the PNIPAM-co-GMA domains swell at least 25 nm above the level of PGMA domains, as discussed elsewhere.[39] This characteristic length is defined by the size of the cell integrin complex responsible for cell binding and can be applied to the cells with the integrin complex intact. However, when the integrin complex has not yet been regenerated for recently harvested cells, this characteristic length may change.

Cell sorting based on their adhesiveness to the coating can be approached experimentally if weakly adhesive cell A is pushed off the surface by the swollen PNIPAM-co-GMA domains while stronger-bound cell B remains on the surface. Consequently, for cell sorting of a mixture of cells A and B, the push-off force (POF) generated by the swollen domains should be above the adhesive force of cell A (AdA) and below the adhesive force of cell B (AdB), or AdA<POF<AdB. This requirement is applied to the one-step or periodic sorting method, which includes the assumption that all cells are uniformly adhered to the surface. For a continuous process, the condition is POF>AdB>AdA. Obviously, this condition assumes the detachment of all the surface-bound cells, but differs in the kinetics of the detachment. Additional requirements should be added to realize continuous sorting. However, this paper focuses on one-step sorting to enable it to be a precursor and optimization step of a future continuous process. Notably, the advantage of the thermoresponsive surface is the uniformity of the osmotic swelling independent of the arrangement and geometry of the supporting basal surface.

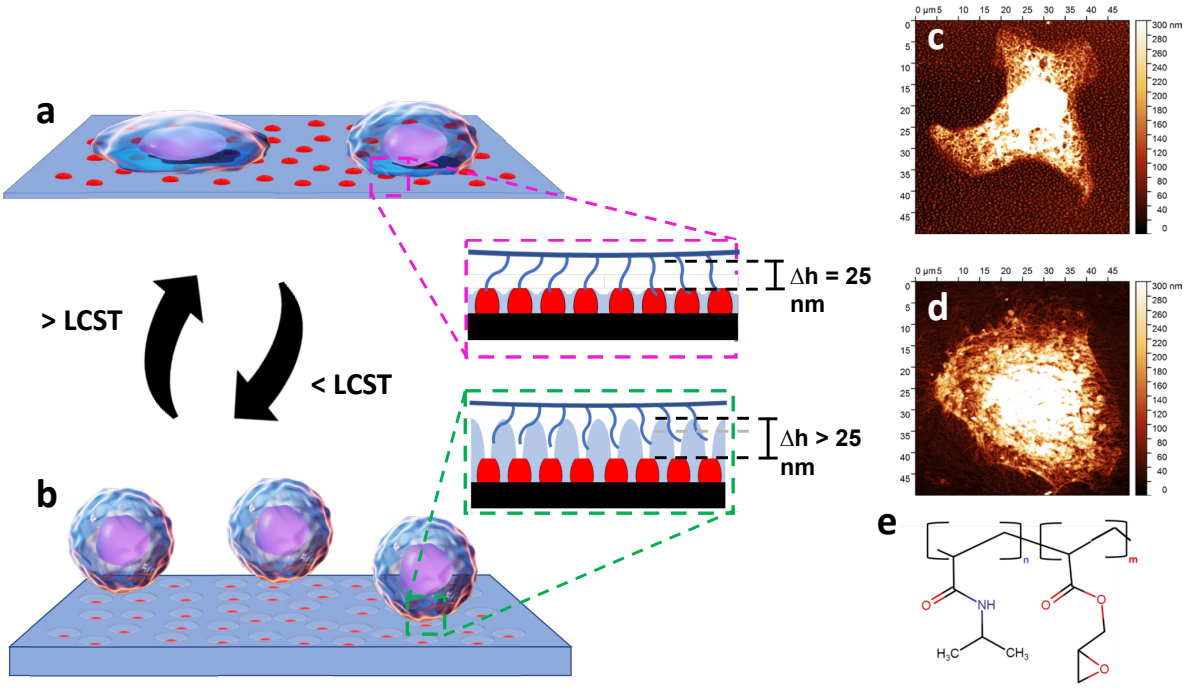

Figure 1. The concept of cell sorting. (a,b) Schematic of the microstructured surface red (PGMA domains) & blue (PNIPAM-co-GMA matrix), as it undergoes changes with temperature and achieves varying detachment of different cell types to promote cell sorting. (a) The PNIPAM matrix is in the collapsed state and facilitates nonspecific cell adhesion to PGMA domains at regular incubation temperatures above LCST. (b) The PNIPAM matrix swells to push off weaker adhered cells when the temperature drops below LCST. The insets (a) and (b) underline the critical length scale characteristics for (a) swelling of the PNIPAM domains: 25 nm is the length of the cell integrin binding complex. (c,d) Insets are SPM images of the cells (c) bound to the microstructured surface and (d) bound to the reference PGMA surface. (e) Chemical structure of the matrix copolymer with 5% wt of GMA monomeric units.

3.2. Fabrication of the microstructured surfaces: experiments and simulations. Approaching the AdA<POF<AdB condition depends on the height ratio of the PNIPAM-co-GMA domain to the PGMA domains, crosslinking density of PNIPAM-co-GMA domains, and the lateral dimensions of the domains or surface coverage by the domains. The first goal is to explore these three adjustable factors for the fabrication of microstructured coatings with tunable POF. The second goal is to replace costly lithographic methods with a simple and scalable method of fabrication based on the phase separation of two polymers during film formation that can be applied to larger surface areas using spin-coating or dip-coating technologies. The microstructured surfaces were fabricated in two steps. In Step 1 (Figure S6), the mixture of PNIPAM and PGMA in dioxane was spin-coated on the surface of the Si-wafer. The phase separation upon solvent evaporation results in the formation of microstructured films when the phase separation is frozen upon the vitrification of the polymers. The structure of the film and the domain dimensions depend on the miscibility characteristics of the polymers, their ratio in the

mixture, the solvent, and the conditions of spin-coating. Many of these parameters are found empirically in experiments. After deposition, solely the PGMA domains were thermally partially crosslinked (to provide the PGMA domain stability in the following steps) with a short time (3 min) annealing at 150 °C, while PNIPAM was not crosslinked, purposely to allow subsequent steps. The ratio between the two polymers in solution was PNIPAM:PGMA>1 to ensure the formation of a PNIPAM matrix and PGMA island domains.

An equivalent model system was obtained in the form of phase-separated surface tethered polymer chains at conditions of strong repulsion between the PGMA and PNIPAM polymers in the *θ*-solvent for a range of the mass fractions, *f,* of PGMA. The result is illustrated with a sequence of snapshots at the substrate level in Figure 2. The PGMA and PNIPAM domains are displayed in orange and magenta, respectively. A solvent is not shown to avoid clogging.

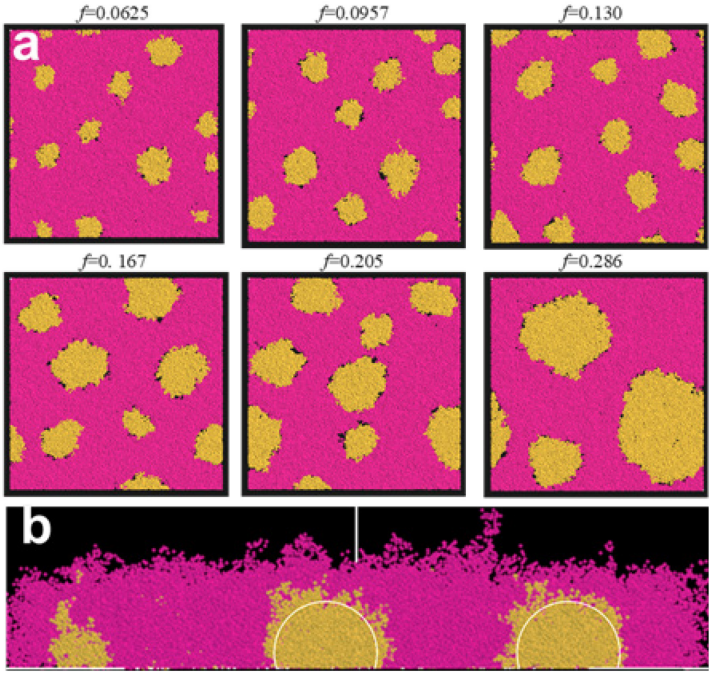

Fi**gure 2.** Computer simulation snapshots of the phase-separated PGMA/PNIPAM film in the form of a tethered polymer layer for different mass ratios of PGMA, *f*. Simulation time $5 \cdot 10^5$ DPD steps (a) substrate-level view, (b) side view *f*=0.167. White circles represent the spherical cap shape of the PGMA domains.

In Step 2 (Figure S7), the phase-separated film was rinsed in water to extract PNIPAM, resulting in PGMA spherical cap structures decorating the surface. Then, different concentrations of PNIPAM-co-GMA solutions were used to refill the gaps between PGMA domains using the spin-coating method. Higher concentrations of the copolymer resulted in a thicker PNIPAM-co-GMA matrix. We experimentally found a range of concentrations to fabricate the thin film coatings with

different ratios of PGMA domain heights and PNIPAM-co-GMA matrix thicknesses. The deposition of PNIPAM-co-GMA resulted in the formation of a thin film coating over PGMA domains, which blocks direct PGMA access. It was etched with plasma for 1 min (Figure S10 and Figure S11) to remove this thin layer. We prepared a series of samples by varying the concentration of PNIPAM/PGMA mixtures in Step 1 to vary the size of PGMA domains and their height. We varied the concentration of PNIPAM-co-GMA in Step 2 to vary the PGMA/PNIPAM-co-GMA height ratio.

3.3. Characterization of microstructured surfaces. The fabricated microstructured surfaces were characterized using SPM after Step 1 (Figure S12) and after Step 2 in air and water at temperatures below and above LCST. The representative SPM images and corresponding cross-section are shown in Figure 3. Notably, the swelling of PNIPAM-co-GMA in water at T>LCST is only 10-20%. Consequently, the images underwater at T>LCST and in the air are very similar. The bumpy surface of the coating at T>LCST with PGMA bumps (Figure 3a), seen in profile (Figure 3c) is transformed into a crater-like surface after swelling of PNIPAM-co-GMA matrix (Figure 3b), with the degree of swelling that results in notable coverage of the PNIPAM domains (Figure 3c).

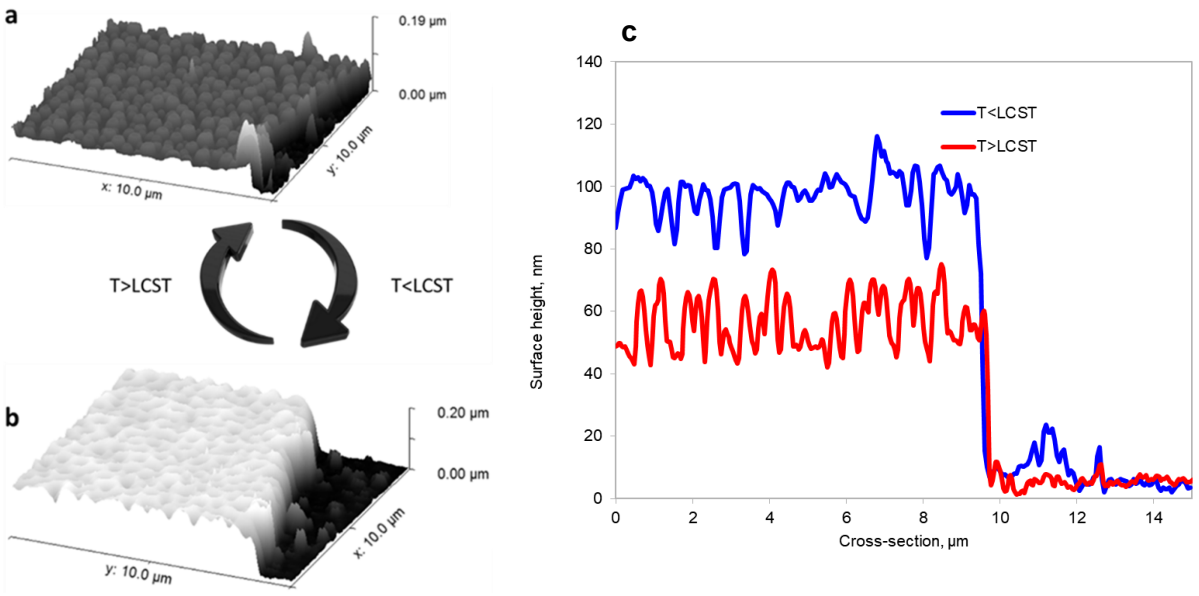

Figure 3. SPM image of a typical microstructured coating in water: (a) T>LCST, (b) T<LCST; and (c) the corresponding cross-sectional profiles (the locations of the profile cross-sections are shown with blue and red lines on (a) and (b) panels).

The SPM data were analyzed to extract the dimensional characteristics of the microstructured surfaces. It was essential to obtain statistical analysis of the major dimensional characteristics

because of their critical role in cell sorting. In this analysis, we modeled the PGMA domains using the spherical cap geometry schematically shown in Figure 4. The spherical cap model was used to characterize the microstructured surfaces after Step 1, which includes partial crosslinking, and after Step 2, which includes plasma treatment, to monitor different stages of the fabrication.

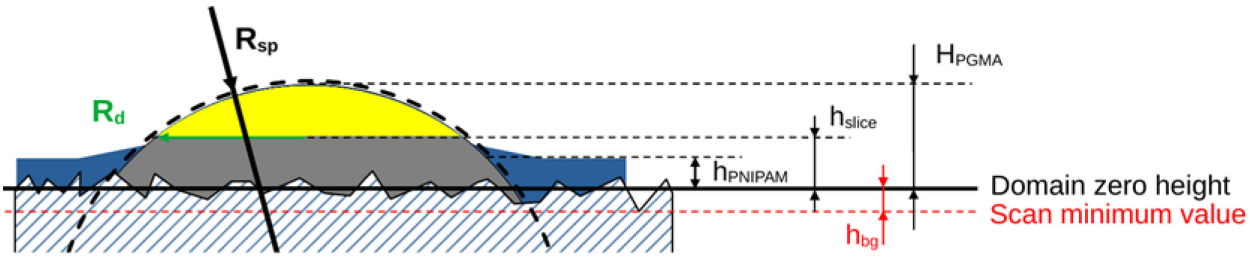

Figure 4. Schematic of the cross-section of a PGMA domain: h_{bg} is the roughness of the basal surface, typically 3-7 nm; h_{slice} and H_{PGMA} were measured from the scan minimum value, and then h_{bg} was subtracted to set the background to zero. h_{PNIPAM} is the height of the PNIPAM-co-GMA matrix; h_{slice} is the height of a virtual slice, with the yellow-colored area above the slice; H_{PGMA} is the maximum height of the domain, taken as a median of maximum heights for all domains; R_{sp} is the sphere's radius with the same curvature as the domain, taken as an average of the median largest and the median smallest curvature radii for all domains. R_d is the radius of a disc with the same projected area, estimated as a median for all domains.

The choice for the spherical cap geometry was supported by the analysis of the PGMA domain shape using experimental and simulation data. The SPM images and simulation data were used to slice the PGMA domains parallel to the substrate plane and compare the experimental and simulation geometry with the geometry of the spherical cap (Table S1). We may draw several conclusions from this data. Firstly, for the experimental data, the spherical cap approximation for the PGMA domains works very well, as the individual radii, R_{sp}, are very close for various slices of the same sample. The values of R_d, measured in the experiment, and the values of R_d' for the spherical cap geometry are also very close. Secondly, the domains' average radius and average height increase approximately linearly with the fraction of PGMA, *f*. The accuracy of the simulation data is lower, and we attribute this to the moderate system size. From the comparison of the experimental and simulation data (H_{PGMA}), we found the length scaling factor of $\sigma \approx 9$ nm (see SI Modeling part). Then, we note that matching the R_d values requires a factor about 4 times larger than that, namely, $\sigma' \approx 36$ nm. This means that the simulation domains are less “immersed” in the substrate than in the experimental structures, which is also visualized in Figure 2b. We can speculate that the latter is attributed to the early stage of phase separation in the case of simulations. Another possible reason for the discrepancy between the experimental and simulation results for the PGMA shape is the role played by the PGMA-substrate interaction. This can be addressed in future studies.

The several fabrication steps of thermal annealing and plasma treatment lead to changes in the dimensions of the initially formed domains (Table 1 and Table S2). The SPM scanning was repeated for the microstructured surfaces after plasma treatment to obtain the characteristics of the surfaces used for cell sorting. The dimensions of the domains in the microstructured surface fabricated in Step 2 are shown in Table 1. The height distribution for PGMA domains after Step 1 and after Step 2 is shown in Figure S13 and Figure S15, respectively. The height distribution of PNIPAM domains is shown in Figure S14. The changes in height distribution for the microstructured surfaces caused by swelling of the PNIPAM-co-GMA matrix are shown in Figure S16. The results show a very broad distribution by height of PGMA domains and a narrow height variation for PNIPAM-co-GMA matrix.

Table 1. Structural characteristics of the microstructured surfaces: H_{PGMA} air is the median of the highest points of PGMA domain in air, with the inter-quartile range in parentheses; h_{PNIPAM} air is the height of PNIPAM layer in air, with the variance in parentheses; h_{PNIPAM} below LCST is the height of PNIPAM layer in H_2O at 24 °C, with the variance in parentheses; d is the distance between domains centers, averaged over four nearest domains; ρ is the number of domains per 1 μm^{-2}; A is the median of the domain area above PNIPAM layer in air, with the inter-quartile range in parentheses; ρ×A is the surface coverage by PGMA domains exposed above PNIPAM at T>LCST.

Sample	H_{PGMA} air, nm	h_{PNIPAM}, air, nm	h_{PNIPAM} below LCST, nm	Swelling ratio	d, nm	ρ, μm^{-2}	A air, μm^2	ρ×A
A0	104.5 (66.6)	-	-	-	494 (84)	3.9	-	-
A1	57.1 (13.6)	16.7 (2.9)	57.7 (6.8)	3.5	502 (96)	3.7	0.17 (0.10)	0.58
A2	72.8 (6.7)	51.5 (2.3)	113.2 (6.6)	2.2	532 (87)	3.5	0.125 (0.11)	0.51
B0	76 (19.7)	-	-	-	384 (65)	6.4	-	-
B1	41.5 (7.4)	19.4 (1.8)	40.0 (3.2)	2.1	377 (75)	6.5	0.076 (0.055)	0.49
B2	63.7 (7.0)	41.7 (1.8)	91.7 (5.9)	2.2	400 (68)	6.1	0.075 (0.055)	0.45
C0	52 (18.7)	-	-	-	357 (73)	7.0	-	-
C1	32.6 (5.8)	15.9 (1.5)	33.1 (4.2)	2.1	354 (72)	6.8	0.045 (0.033)	0.31
C2	58.6 (4.1)	45.1 (1.4)	95.3 (5.3)	2.1	374 (66)	7.2	0.055 (0.032)	0.40

*A, B, C denote PGMA:PNIPAM-co-GMA ratio; 1 and 2 correspond to two different PNIPAM-co-GMA film thicknesses (Step 2); 0 denotes the samples received after phase separation, short annealing, and washing out PNIPAM (Step1).

3.4. Swelling PNIPAM matrix.

DPD simulations were performed to address two questions: 1) the effect of the crosslinking on the swelling of the surface grafted PNIPAM-co-GMA matrix and 2) the effect of the microstructured surface geometry and pining (grafting to PGMA domains) on the swelling of the PNIPAM-co-GMA matrix.

The repeating unit of PGMA and PNIPAM chains are treated as a single soft bead of roughly 10 atoms each, as shown in Figure S17. Details of the models are discussed in SI (Figures S18-S20). Initially, we performed crosslinking of the PGMA domains. To this end, all its beads are considered initially active and accessible for crosslinking. It occurs with a probability of 0.1 if the pair of active beads touch or interpenetrate each other's soft core. After the crosslink is registered, both beads are exempt from the following crosslinking attempts. The crosslinking lasted $50 \cdot 10^3$ DPD steps, and the number of crosslinks saturated at the end. Because of the vast number of active GMA groups in PGMA, the PGMA domains are practically solidified. In the next step, the voids between PGMA domains are filled by the PNIPAM-co-GMA copolymer, which is also crosslinked. For this purpose, we assume 5% of its beads to be of the GMA type.

To examine the effect of the PNIPAM-co-GMA crosslinking on its thermoresponsive properties, we performed a simulation for the surface-grafted PNIPAM-co-GMA crosslinked in the collapsed state. Three grafting densities, ρ_g=0.2, 0.4 and 0.6, were examined. The crosslinking fraction of PNIPAM-co-GMA was defined as $v_{cr}=2N_b/N_{pnipam}100\%$, where N_b is the number of formed crosslinking bonds, and N_{pnipam} is the total number of PNIPAM-co-GMA polymer beads. Here, the initial fraction of GMA was 30%, and uncrosslinked beads transformed into PNIPAM after the needed v_{cr} was reached. The average PNIPAM-co-GMA matrix height below LCST is denoted as h_1, whereas its counterpart above LCST as h_2. In all cases, an increase in crosslinking fraction, v_{cr}, leads to a decrease of the swelling ratio, h_1/h_2, and the effect is more significant at lower grafting density ρ_g, (Figure 5).

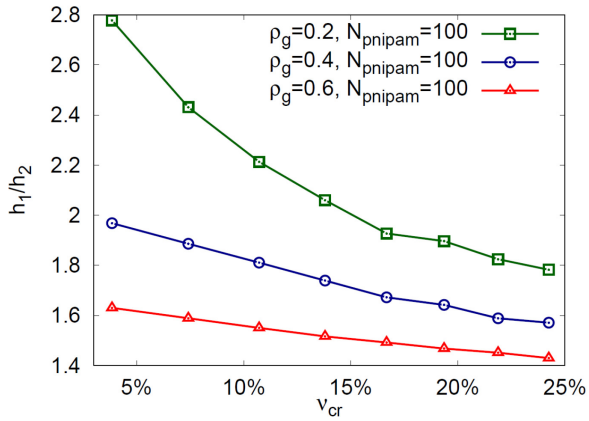

Figure 5. The effect of the crosslink fraction, v_{cr}, on the swelling ratio h_1/h_2, i.e., between the PNIPAM-co-GMA matrix height below and above LCST. Three different surface grafting densities, ρ_g=0.2, 0.4, and 0.6, were analyzed.

The parameters of the model N_{pnipam}=100, ρ_g=0.2, and a crosslinks fraction in a range of v_{cr}=5-7% lead to the swelling ratio of about 2.4-2.8, which is in accord with the experiments (Table 1).

Another problem relates to grafting PNIPAM-co-GMA matrix to PGMA domains via reactive epoxy groups in both polymers. Such grafting can potentially restrict swelling of PNIPAM-co-GMA. The DPD method was applied to perform simulations for microstructured surfaces with the geometry of a spherical cap (Figure 4) obtained in the experiments. The PGMA solid domains in our model were considered as two spherical caps on opposite sides of the simulation box. In between the domains is the substrate covered by PNIPAM-co-GMA. We considered a narrow simulation box, so the curvature of the spherical caps along the width is not significant; this allows us to save computational resources and also to focus on a smaller set of parameters. The PNIPAM can be pinned to the substrate, and the domains have an independent density of pinning points. The pinning density to the substrate was fixed to be ρ_g=0.2, and for the domains, three possibilities ρ_{pd}=0.2, 0.4, 0.6 were considered. The radii of the spherical cap were R=30, 50, and 100, and in each of these cases, the spherical cap height was 10, and the maximal height where PNIPAM-co-GMA can be pinned was also kept fixed as 7. The separation between domains, s, the distance between nearest points on the domains at the level of the substrate, was considered as s=10, 20, 30, and 40. In Figure 6, we show instantaneous frames from the simulation for the case R=100, s=40. Other parameters of the model can be found in SI.

The results of the simulations are shown in Figure 6. There is little variation for the different radii (Figure 6d). The swelling ratio h_1/h_2 increases with the separation distance increment (Figure 6e). An increase in the crosslink fraction v_{cr} from 7% to 14% leads to a lower swelling ratio but does not affect the qualitative behavior significantly. On the other hand, the swelling ratio notably

decreases when the pinning density on the domains, ρ_{pd}, increases from 0.2 to 0.6. This effect is more significant than any considered variations in radii or crosslinking fraction.

Before the discussion of cell sorting on the microstructured surfaces we can draw the major conclusions from the characteristics of the microstructured surfaces: 1) a relatively narrow distribution of spacing between PGMA domains that can be adjusted by the concentration of solutions for spin-coating; and 2) a broad distribution in the height of PGMA domains, which is important to consider for analysis of cell-sorting experiments; 3) a narrow distribution of the PNIPAM matrix height; 4) the size of the PGMA domains and the surface coverage available for cell binding to the PGMA domains increases with the PGMA fraction in spin-coating solutions in Step1; 5) the height of the PNIPAM-co-GMA domains in A1, B1, and C1 samples at T<LCST is very close to the height of PGMA domains at T>LCST (a low POF is expected), while for A2, B2, and C2 samples the structure is substantially different and a high POF is expected; 6) PNIPAM-co-GMA matrix swelling is less dependent of the domain geometry but depends on the matrix crosslinking density, surface grafting density, and distance between domains.

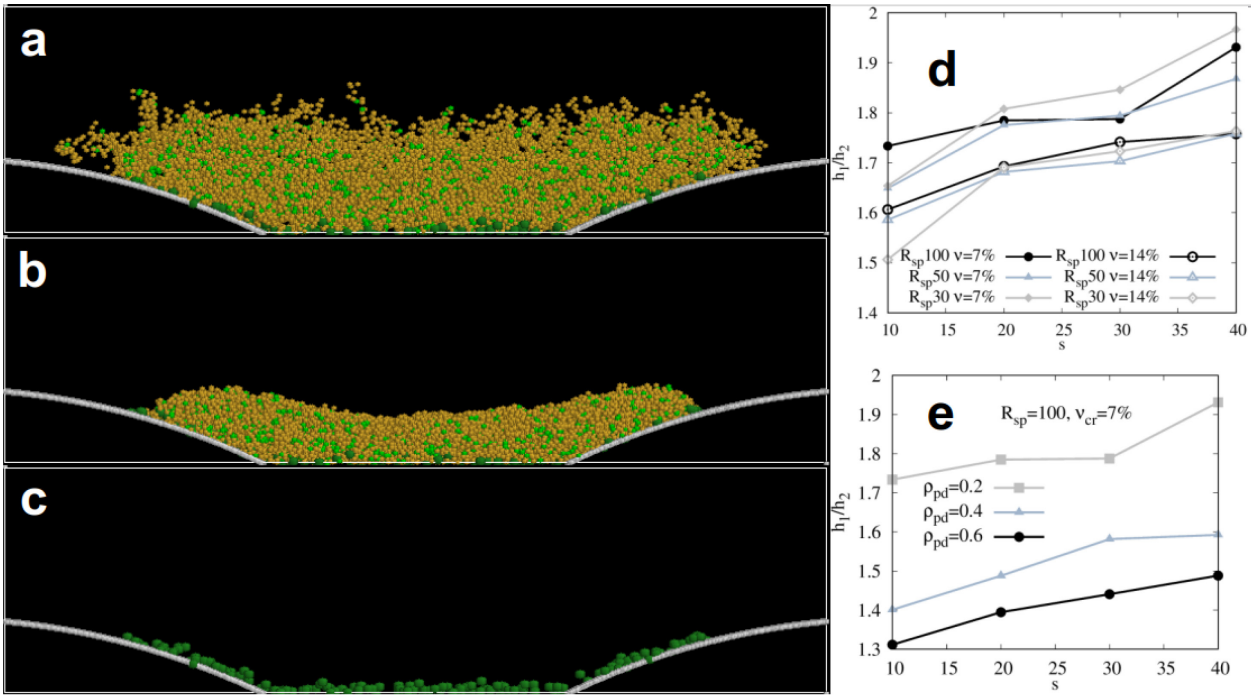

Figure 6. The simulation box with spherical domain caps and crosslinked PNIPAM-co-GMA matrix pinned to the substrate and domains (R=100 and s=40): (a) T<LCST, (b) T>LCST). The yellow beads represent PNIPAM; light-green beads are crosslinking GMA points; and dark-green beads are pinned points; (c) only pinning points are shown; (d) dependence of swelling on separation distance, s, for different R; (e) dependence of swelling on separation distance, s, for

different surface grafting densities ρ_{pd}. Note that the results in (d) and (e) are not for the fully equilibrated network, see SI.

3.5. Cell sorting. Monte Carlo simulations.

We performed Monte Carlo computer simulations for the above-described model for the binary mixture of cell types 1 and 2 at the four different micropatterned surfaces, which differ by PGMA domain size. We consider four values of the domain diameter D_d=2R_d (Figure 4) in reduced units ($D_{\mathrm{d}} = 0.5,\ 1.0,\ 1.5,$ and 2.0), while the coverage fraction of the surface by the PGMA domains was fixed and equal to $\sigma_{\mathrm{d}} = 0.48$. Cells 1 and 2 differ only by the strength of attraction to the domains by the adhesion parameters $A_{1d} = -0.4$ and $A_{2d} = -0.3$, respectively.

For each surface, simulations were performed in two sequential stages: cell adsorption and desorption. We considered the equivalent number of cells of both types in the system equal to $N_1 = 100$ and $N_2 = 100$. At the beginning of the first stage, cells were randomly distributed within the simulation box and subsequently allowed to move stochastically, adhering to the domains upon encountering the surface, when the parameter of repulsive interaction of a cell with the polymer phase was $B_p = 0.0$, i.e., the PNIPAM-coGMA was in the collapsed state and did not repel the cells. The adsorption stage consisted of 2M simulation steps; however, adsorption is typically completed within 200K to 500K steps. To ensure that the system had reached a stationary regime, the potential energy of the cells was monitored to verify its saturation. As a result, all cells were adsorbed onto the surface ($B_{\mathrm{p}} = 0.0$), forming a monolayer with a surface density of $\rho_{\mathrm{c}} = (N_1 + N_2)/L^2 = 3.472 \cdot 10^{-3}$, corresponding to a surface packing fraction of 0.273. This indicates that cell crowding at the surface was negligible and that competition for available adhesion sites was minimal. A movie generated from our computer simulation illustrating the typical adsorption stage can be found in SI Video 1. All snapshots and movies obtained from our simulations are created with the help of OVITO software.

In the second stage, the final configurations obtained during the first stage were used to initiate the desorption process by applying a repulsive field induced by the swollen polymer phase. This was achieved by varying the parameter B_{p}. The desorption stage was conducted for 2M simulation steps, although the system typically reached a stationary regime much earlier. In SI (Figure S25 and Figure S26), we demonstrate snapshots for the case of the domain sizes $D_{\mathrm{d}} = 0.5$ and 2.0, respectively. It is clearly observed that an increase in B_{p} results in greater cell detachment. Moreover, a higher number of type 1 cells remains at the surface, while type 2 cells predominate in the environment. A movie generated from our computer simulation illustrating the

typical desorption stage can be found in SI Video 2. It can also be noticed that cell detachment is more pronounced in the case of the smaller domains; however, a quantitative analysis is required to confirm this observation, which is presented below.

Based on the cell trajectories obtained from our simulations, the density profiles for both cell types were calculated and averaged over 1M steps. Using these density profiles, the average number of cells located within a cutoff distance $r_{\mathrm{cut}} = D_1/2$ (or $D_2/2$) from the surface were estimated for various values of D_{d} and B_{p}. This approach allowed us to assess the efficiency of cell sorting under different conditions. In Figure 7a, we present the fractions of cells remaining attached to the surface, expressed as percentages. It can be seen that both types of cells undergo detachment as B_{p} increases. However, for type 1 cells, detachment is less pronounced and occurs with a significant delay along the B_{p} compared to type 2 cells, resulting in a cell separation. The efficiency of this separation can be assessed using the separation factor, which reflects the relative amounts of the two cell types attached to the surface vs. the initial adsorption ratio 1:1. We present this factor in Figure 7b as a function of the parameter B_{p}, exhibiting a non-monotonic dependence.

Assuming that a higher separation factor corresponds to better separation efficiency, the maxima of the curves obtained for different sizes of adhesive domains should indicate the values of B_{p}, at which optimal separation performance is achieved. Interestingly, for larger domains, these maxima are higher than those for smaller domains and occur at higher values of B_{p}. For instance, when the domain size is $D_{\mathrm{d}} = 0.5$, the maximum occurs around $B_{\mathrm{p}} = 0.32$, while for $D_{\mathrm{d}} = 2.0$ it is around $B_{\mathrm{p}} = 0.37$. It is worth noting that for $B_{\mathrm{p}} = 0.32$ and $D_{\mathrm{d}} = 0.5$, about 35% of type 1 cells and nearly 3% of type 2 cells remain attached to the surface. Approximately the same 35% of type 1 cells can be found for $D_{\mathrm{d}} = 2.0$ at $B_{\mathrm{p}} = 0.37$, while the fraction of type 2 cells is slightly lower ($\sim 2.5\%$) than for $D_{\mathrm{d}} = 2.0$ at $B_{\mathrm{p}} = 0.32$. Nevertheless, this small difference is sufficient to increase the separation factor by about 20% when the domain size is increased from $D_{\mathrm{d}} = 0.5$ to $D_{\mathrm{d}} = 2.0$. It should be noted that this effect is analyzed under the fixed coverage fraction of the surface by the PGMA domains. The interplay between domain size and surface coverage remains a promising direction for future research.

To summarize, the choice of domain size plays an important role in cell sorting and should be taken into account even when the coverage fraction remains the same. We found that increasing the domain size can enhance the efficiency of cell sorting. Another important parameter – the repulsion strength or POF, which depends on the polymer phase density, must be carefully

adjusted to achieve a fine balance with the adhesive properties of the domains, domain sizes, and the coverage fraction. The model developed in this study, based on Monte Carlo simulations, can assist in identifying consistent and reasonable values for these parameters.

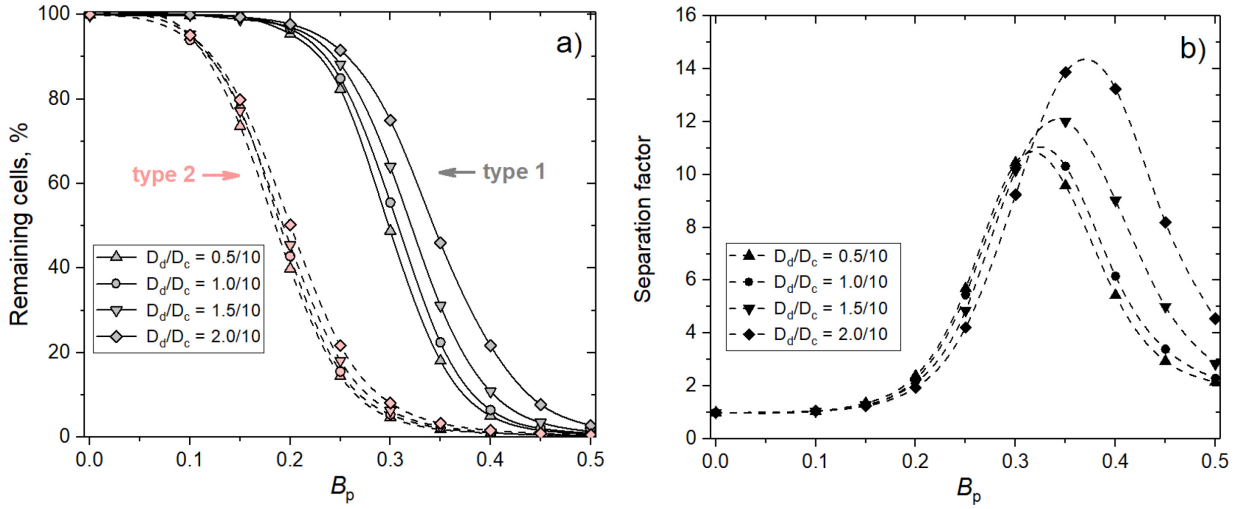

Figure 7. Results of computer simulations: (a) **r**emaining cells on the surface and (b) separation factor simulation data as a function of the PNIPAM-co-GMA polymer-cell repulsion parameter B_p, for different PGMA domain diameters $D_d = 0.5, 1.0, 1.5$, and 2, at a surface domain coverage of $\sigma_d = 0.48$. Adhesion parameters of cells of type 1 and 2 are equal to $A_{1d} = -0.4$ and $A_{2d} = -0.3$, respectively.

Microstructures with bigger PGMA domains exhibit higher sorting efficiency; however, the outcome also depends on the strength of the repulsive force exerted by the polymer phase. If the repulsion is too weak or too strong, the sorting process becomes ineffective.

3.6. Cell sorting experiments. The fabricated microstructured surfaces were tested in a series of experiments that can be divided into two groups. In one group, cells were seeded on the surface and incubated for a “short” time of 20 min, while in another group, the incubation time was “long” 16 h. For HaCaT cells, 20 min incubation time was not sufficient to bind cell to the surface, so we increased the incubation time to 1 h instead of 20 min. These differences are to probe cell sorting at different stages of cell adhesion. In each group, we probe microstructured surfaces for adhesion and detachment of individual cells and their mixtures.

The cells were seeded at 37 °C, and after incubation in a CO_2 incubator, they were visualized on the surface at 37 °C and after cooling down to room temperature T<LCST. One component PGMA and PNIPAM-co-GMA films were used as controls. The poorly bound cells were suspended using either gentle pipetting or directed media flow using a peristaltic pump (PP). Pipetting is broadly used to collect loosely attached cells, but even gentle pipetting can develop a noticeable shear

force acting on the cells. This force will add to POF. The impact of the shear flow was minimized by using a media flow of about 4 ml/min generated by the peristaltic pump flow (Figure S10).

We used 3T3, HaCat, and RAW cells, which are well-known to have different adhesive properties. RAW cells are more adhesive to standard cell culture materials (plasma-treated polystyrene dishes), compared to 3T3 and HaCaT. The representative images for 20 min and 16 h incubation times for a 3T3 and RAW cell mixture on the microstructured surface A1 are shown in Figures 8 and 9. For both incubation times, cells strongly adhered to PGMA control surfaces and did not detach at T<LCST, while the cells did not attach well to PNIPAM-co-GMA control coatings at 37 °C.

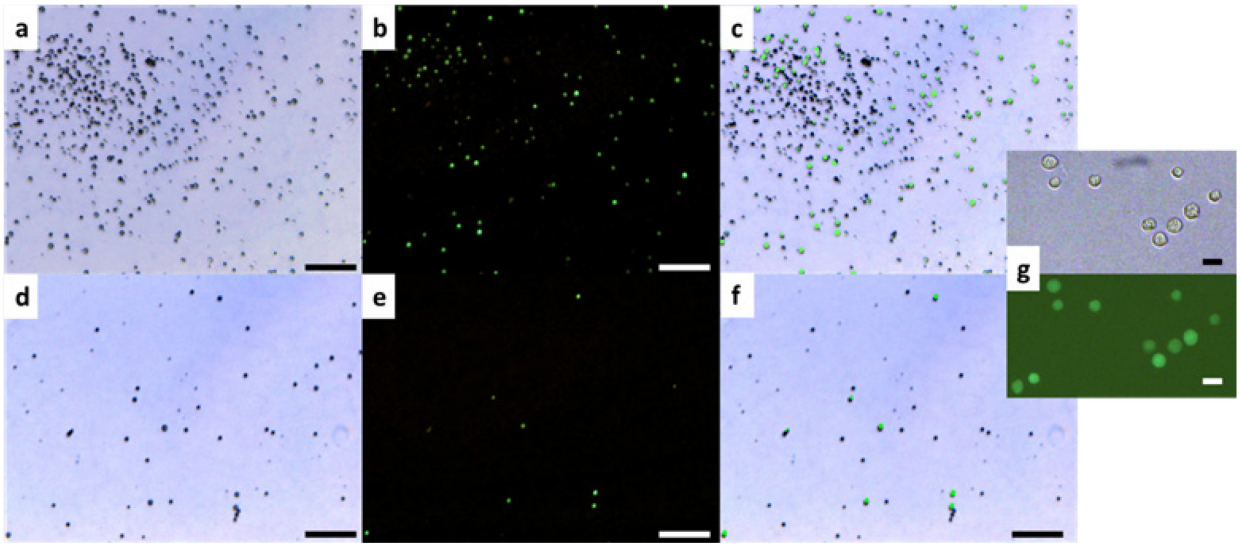

Figure 8. Optical images of a mixture of RAW and 3T3 cells on the microstructured A1 surface: (a-c) after 20 min incubation at 37 °C (T>LCST), and (d-f) after cooling to room temperature (T<LCST) and pipetting: (a,d) no fluorescent filter applied; (b,e) fluorescent filter applied to visualize only 3T3 cells; (c,f) overlay of (a) and (b), and (d) and (e) images, respectively; (g) zoomed up images of 3T3 cells on the microstructured surface after 20 min incubation; (a-f) scale bars are 200 μm; (g) scale bar is 20 μm.

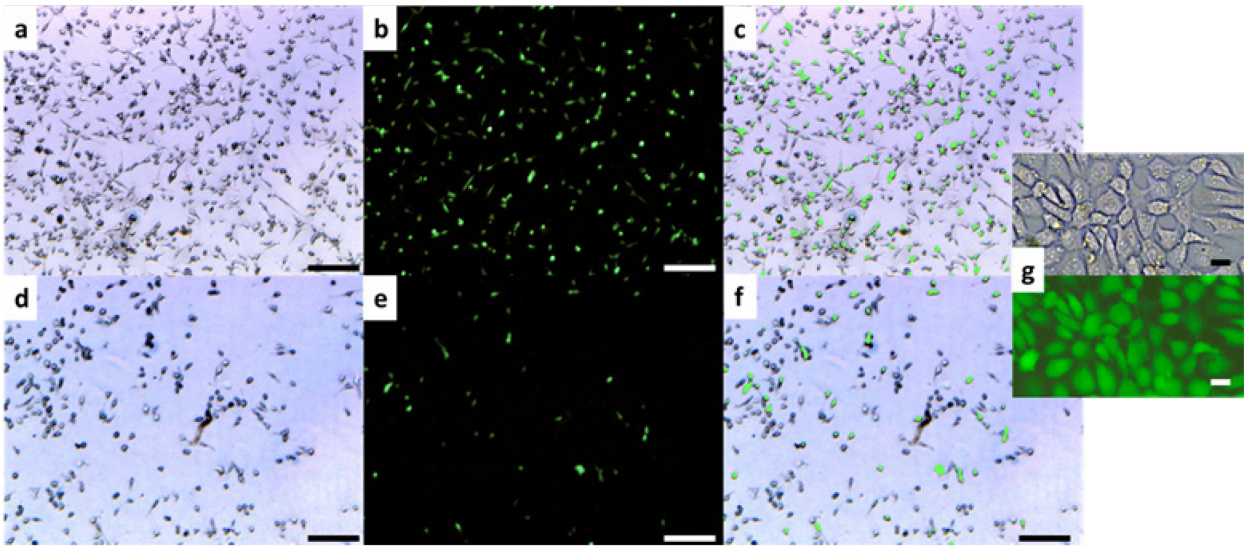

Figure 9. Optical images of a mixture of RAW and 3T3 cells on the microstructured A1 surface: (a-c) after 16 h incubation at 37 °C (T>LCST), and (d-f) after cooling to room temperature (T<LCST) and pipetting: (a,d) no fluorescent filter applied; (b,e) fluorescent filter applied to visualize only 3T3 cells; (c,f) overlay of (a) and (b), and (d) and (e) images, respectively; (g) zoomed up images of 3T3 cells on the microstructured surface after 20 min incubation; (a-f) scale bars are 200 μm; (g) scale bar is 20 μm.

From Figures 8 and 9, it is evident that 3T3 cells adhere more weakly to the microstructured surface than RAW cells. The number of cells that adhere to the surface under T>LCST conditions at 20 min is significantly less than the number of cells observed after 16 h. After 20 min, the cells are weakly bound, and their shape is unchanged (Figure 8g). After 16 h, the cells are strongly bound and elongated (Figure 9g). The increased amount is due to the cell division on the surface. For both incubation times, after cooling to T<LCST, a high fraction of 3T3 cells detached from the surface. For the quantitative evaluation of the sorting efficiency, we used the separation factor (SF) and the percentage of the total number of remaining cells (both types of cells). SF= N_{1i}/N_{2i}:$N_{1s}/N_{2s,}$ where N_{1i} and N_{2i} are the initial numbers of cells type 1 and 2 in the mixture after binding to the surface, N_{1s} and N_{2s} are the numbers of cells type 1 and 2 on the surface after separation (cooling). The ratios of RAW:3T3 cells prior to cooling and after cooling were obtained using image analysis, and the results are shown in Figure 10 (used pipetting) and Figure 11 (used PP flow).

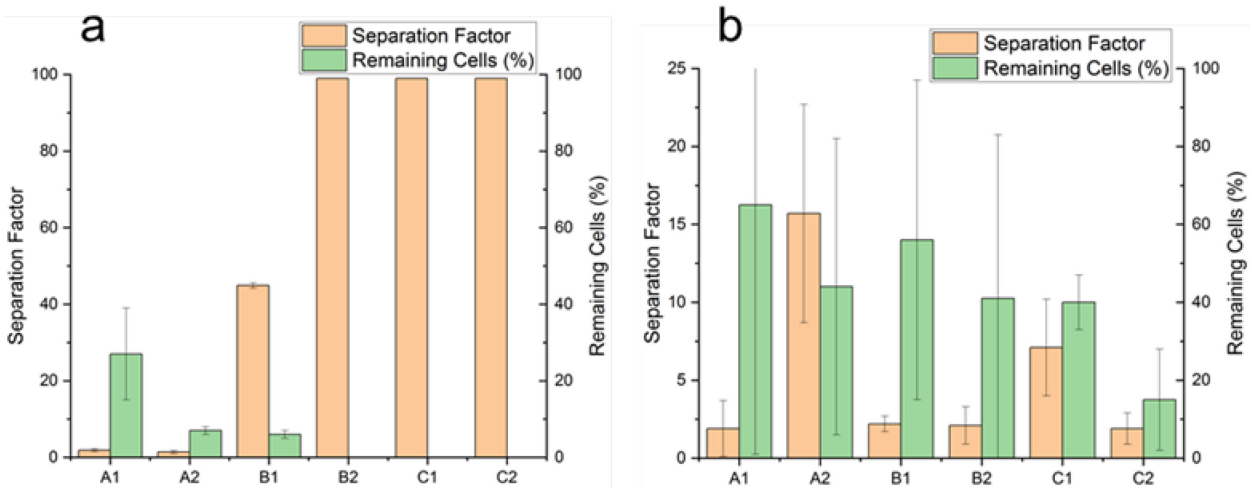

Figure 10. Sorting RAW:3T3 mixtures after (a) 20 min and (b) 16 h incubation; pipetting. The Separation factor (orange) and remaining cell percentages (green) are shown following pipetting and detachment at room temperature (T<LCST) from A1-C2 surfaces.

The results for the control surfaces, namely single-component PGAM and PNIPAM, are not shown in Figure 10 because all seeded cells remained on the PGMA surface, and all cells were removed by pipetting from the PNIPAM-co-GMA surface, resulting in a separation factor of 1. For microstructured surfaces, we observed the separation factors greater than 1 for both incubation times, but the sorting efficiency was greater for 20 min incubation time (weaker cell binding).

With a decrease in the PGMA:PNIPAM-co-GMA ratio, A>B>C samples (less PGMA used), the PGMA domains become smaller, leading to the reduction of the surface coverage by PGMA domains for binding cells (Table 1). Hence, the weakly adhered 3T3 cells are easily removed by the POF. Consequently, a high RAW:3T3 ratio on the surface is achieved (Figure 10a), demonstrating not only effective sorting, with a separation factor of 99 but also causes the surfaces to be so repelling that a very limited number of remaining cells was observed, although those that remained were nearly exclusively RAW cells. This is exacerbated when A2, B2, and C2 samples are used in comparison to A1, B1, and C1 when PNIPAM-co-GMA swelling (T<LCST) exceeded substantially the height of the PGMA domains (high POF). The swollen PMIPAM-co-GMA matrix exceeds the PGMA domains in A2, B2, and C2 samples by a much greater than the 25 nm integrin binding distance. The most extreme case was observed for C2 samples when, after 16 h incubation, <20% of cells remained on the surface with a low separation factor of about 2 (Figure 10b).

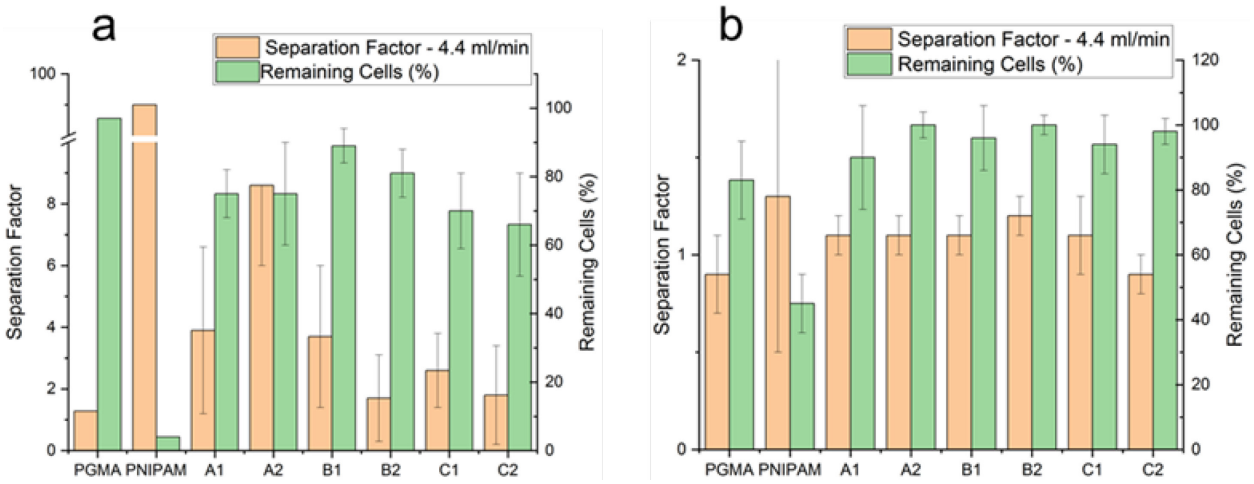

Figure 11. Sorting RAW:3T3 mixtures after (a) 20 min and (b) 16 h incubation; PP flow. The Separation factor (orange) and remaining cell percentage (green) are shown following PP (4 ml/min) and detachment at room temperature (T<LCST) from A1-C2 surfaces.

The data from the experiments with the same cell cultures and microstructured surfaces but with a controlled PP shear flow are shown in Figure 11. The manual pipetting is not well controlled, and hence, it is difficult to reproduce the shear force added to POF. As an indirect measure of the shear force, we used the media flux through the needle. We applied an empirically selected 4 ml/min flow rate. The observed increased amount of the remaining cells on the surfaces proves that using controlled flux vs pipetting provides less added shear force. The results also support the prior statement that short-term weak adhesion favors sorting. The reference data (control samples) with one component PGMA and PNIPAM-co-GMA surfaces are shown in Figure 11. After 20 min incubation time, a large fraction of cells remained on the PGMA surface, resulting in no separation, while almost all cells were detached from the PNIPAM-co-GMA surface (Figure 11a). This effect is significantly diminished in Figure 11b for 16 h incubation time, with PGMA showing a remaining cell percentage of 87% and PNIPAM-co-GMA having 45%, thus illustrating the lessened difference between the control samples, which can only be a result of cell binding and increased adhesion to the surface. However, no sorting was achieved with these surfaces or any microstructured surfaces for 16 h incubation (Figure 11b). All the samples demonstrate sorting factors (about 1) similar to the single-component PGMA surface.

The effect of the microstructured surfaces is similarly easily identifiable in the shorter 20 min incubation period, with A1 and B1 having a separation factor of approximately 4, and A2 having a separation factor of 8. For all microstructured surfaces, the total percentage of cells remaining on the surface exceeds 60%, B1 and B2 being >80%. The best sorting result was obtained for

A2. The reason for this is the large surface areas of the A samples' PGMA domains compared to B and C. Similar to pipetting results, it is clear that a closer domain-to-matrix height is the most effective, with the high PGMA domains offering sufficient binding capacity for the cells, while the higher PNIPAM-co-GMA thickness is equally more effective at swelling to and past the domains to detach cells and sort effectively. Another important observation is the effect of the shear flow. From the comparison of Figure 10 and Figure 11, we can conclude that the drop in shear force (for PP flow) shifted the efficiency of cell sorting from C samples to A samples. That is in accord with the analysis of the effect of the thickness of PNIPAM-coGMA vs PGMA domains. The stronger combined (swollen matrix plus the shear flow) POF becomes less efficient above some threshold, proving our statement that the efficient sorting is for the optimally adjusted POF in a range AdA<POF<AdB.

In our experiments, we did not evaluate cell adhesion quantitatively to establish a correlation between cell adhesion and sorting efficiency, which can be a future development of this research. However, we used an arbitrary evaluation of cell adhesion for three different cell cultures to the surfaces used for this study. This arbitrary evaluation is based on observations during the work with cell cultures. Based on such observation, the cells can be arranged according to adhesion strength RAW>HaCaT>3T3. HaCaT cells need longer initial "short" incubation times compared to 3T3, with most cells not attaching at all after 20 min; however, following 1 h, reproducible binding results were obtained, with HaCaT having slightly better binding than 3T3, and are shown in Figure 12. Surprisingly, such dependence does not directly correlate with the time course of tripsin/EDTA treatment required for complete cellular detachment from plasma-treated polystyrene plasticware. Usually, tripsin/EDTA treatment time for NIH-3T3 cells is about 2.5-3 min, and for HaCaT cells, such treatment time is about 13-15 minutes.

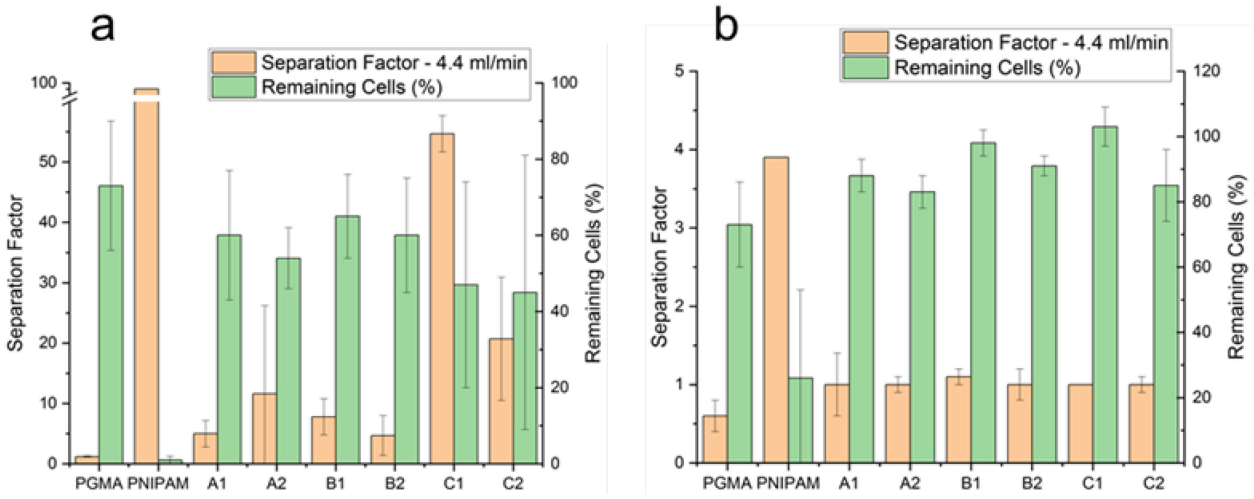

Figure 12. Sorting RAW:HaCaT mixtures after (a) 1h and (b) 16 h incubation; PP flow. The Separation factor (orange) and remaining cell percentage (green) are shown following PP (4 ml/min) and detachment at room temperature (T<LCST) from A1-C2 surfaces.

As can be seen in Figure 12a, the reference surfaces of PGMA and PNIPAM-co-GMA show opposite effects on the separation and removal of cells, illustrated by the percentage of cells that remained, with PGMA having the highest of all surfaces at 73%, which is to be expected, while PNIPAM-co-GMA has almost zero cells remaining, also expected. The separation factor for PGMA is expected to be near 1, which indicates insignificant levels of cell sorting. The microstructured surfaces, on the other hand, show vastly significant separation factors with minimum values ranging from 5-12 for A1, A2, B1 and B2, while C1 and C2 have separation values of 54.7 and 20.7, respectively, which is a very high selection bias, especially considering the number of cells remaining is near 50% in all cases. Similar to RAW:3T3 sorting, however, once cells have been incubated for 16 hours, the effect of the surface structure becomes much less pronounced. Separation is thus again achieved following short incubation periods.

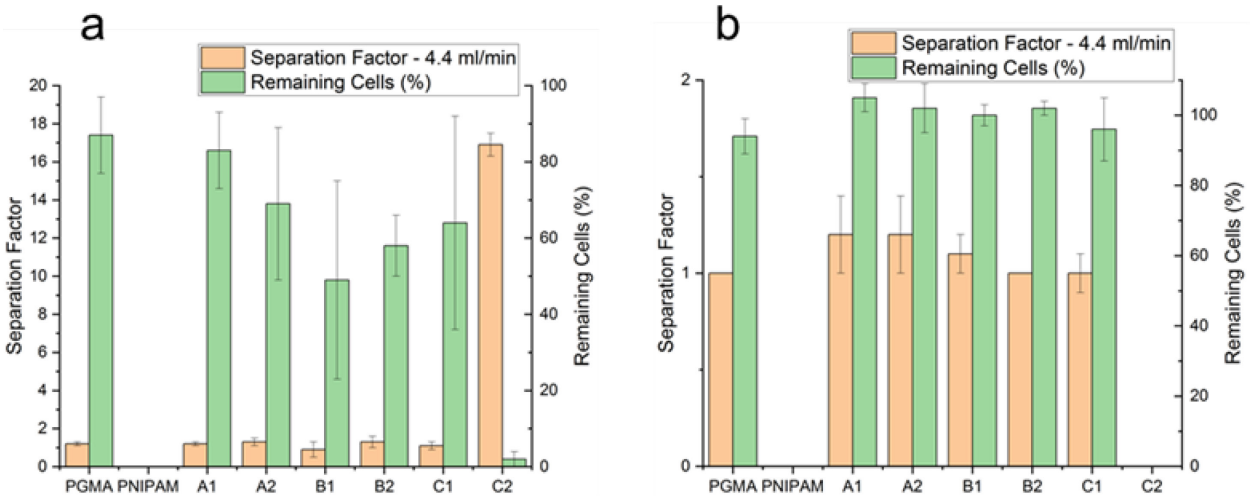

Figure 13. Sorting HaCaT:3T3 mixtures after (a) 1 h and (b) 16 h incubation (PP flow). The Separation factor (orange) and remaining cell percentage (green) are shown following PP (4 ml/min) and detachment at room temperature (T<LCST) from A1-C2 surfaces.

The most difficult task was to sort 3T3 and HaCaT. Both cells are less adherent, and it would be more significant to be able to sort these cells from one another. HaCaT requires 1 hour to adhere to the surfaces; thus, this time served as the minimum incubation time for both cell types in a mixture, while 16 h was still the long incubation period. From Figure 13, it is clear that sorting the cells was not as successful as when either was sorted from RAW cells. Figure 13 shows data reminiscent of both prior sorting experiments when considering the PGMA and PNIPAM-co-GMA reference surfaces with separation factor values of about 1 and nearly 100% remaining cells following sorting for PGMA, while PNIPAM-co-GMA showed excellent cell removal and no separation factor data being calculable from the insignificant number of cells. The microstructured surfaces, however, show a linear SF result regardless of the domains or matrix characteristics, with the only variation being minute at best. The remaining cell percentages in Figure 13a vary to some degree; however, in Figure 13b the variation is negligible. An untested alternative to the experimental results shown in Figure 13 is if an incubation time of less than 1 hour was used. This would have prevented HaCaT attachment and made sorting much more likely. This opens multiple avenues for cell sorting using an identical set of surfaces and can be the basis of future research. The collection of the optical images for the cell sorting experiments can be found in SI cell sorting images file, and the results of the image processing are in Table S3.

4. Conclusions

The experiments and computer simulations provide solid evidence for the feasibility of label-free cell sorting based on weak nonspecific interactions with dynamic stimuli-responsive microstructured surfaces. The separation mechanism based on the adsorption-detachment of cells on and from the microstructured surfaces resembles the chromatography of small molecules when separation is possible at the optimal range of molecule-adsorbent interactions, and the separation of very weakly and very strongly interacting molecules with the adsorbent is not efficient. In other words, if kT is used as a measure of the interaction strength of small molecules with adsorbent, separation is impossible if the adsorption energy is very much lower or greater than kT. In the latter cases, a change of the adsorbent and temperature is used to improve separation. The push-off force on the stimuli-responsive surface plays a similar role for cells as thermal fluctuations for small molecules. The adhesive, PGMA, domains provide cell binding, while thermoresponsive PNIPAM-co-GMA domains push cells off at T<LCST. This combination, if appropriately adjusted so that the push-off force is between the adhesive forces of weakly and strongly bound cells AdA<POF<AdB, the cell separation can be very efficient in terms of separation factor and number of separated cells.

The balance between cell binding and detachment forces is approached by adjusting the surface structure. For the given chemical structure of the adhesive domains, the adhesion can be adjusted by changes in the contact area or surface coverage by the adhesive domains. The kinetics of cell binding is also important. Cell adhesion increases with time. Push-off force can also be adjusted by many factors related to the properties of stimuli-responsive domains: surface coverage, swelling ratio, crosslinking, and the ratio of heights of adhesive and stimuli-responsive domains.

In this work, we successfully separated cells that were substantially different in their adhesive properties from the studied microstructured thermoresponsive surfaces, while the separation of cells with closer adhesive behavior has not yet been successful (a very low separation factor). This problem can be approached by optimizing the geometry of the microstructured surface or using a multistep separation process, and it can be a subject of future research.

Along with the separation mechanism, we also demonstrate a simple method for the fabrication of microstructured thermoresponsive surfaces based on the phase separation of PGMA and PNIPAM-co-GMA copolymers in thin films. The microstructure on the submicron level can be regulated by the ratio of two polymers. The GMA functional groups are used to crosslink the film

and graft it to the substrate. The swelling ratio of the thermoresponsive domain is regulated by the crosslink density, surface grafting density, and geometry of the microstructures. The best combination of these parameters for cell sorting can be predicted with mesoscale computer simulations, which already showed their potential in this study. The developed materials can find applications in scalable and cost-efficient cell sorting technologies.

ASSOCIATED CONTENT

Supporting Information

The Supporting Information is available free of charge at

SI file, which includes schematics of experiments, characteristics of the polymers and microstructured surfaces, and details of models used in computer simulations.

SI Cell sorting optical images.

SI Video 1 Monte Carlo simulation of cell adsorption

SI Video 2 Monte Carlo simulation of cell detachment

AUTHOR INFORMATION

Corresponding Author

Sergiy Minko Nanostructured Materials Lab, University of Georgia, Athens, 30602 USA; https://orcid.org/0000-0002-7747-9668; Email: sminko@uga.edu

Authors

Ronaldo Badenhorst - Nanostructured Materials Lab, University of Georgia, Athens, 30602 United States; https://orcid.org/0000-0001-7276-9554

Sergei V. Makaev - Nanostructured Materials Lab, University of Georgia, Athens, 30602 United States; https://orcid.org/0000-0002-4052-4437

Mikhail Parker - Nanostructured Materials Lab, University of Georgia, Athens, 30602 United States; https://orcid.org/0009-0006-2722-847X

Vladimir Reukov - Department of Textiles, Merchandising, and Interiors, University of Georgia, Athens, Georgia 30602, United States; https://orcid.org/0000-0003-1695-6712

Rostyslav Marunych - Lab of Experimental Biology and Department of Biochemistry & General Chemistry, Faculty of Medicine, Rzeszów University, Warzywna 1a Str., 35-959, Rzeszów, POLAND; https://orcid.org/0000-0002-2246-8988

Agnieszka Będzińska - Lab of Experimental Biology and Department of Biochemistry & General Chemistry, Faculty of Medicine, Rzeszów University, Warzywna 1a Str., 35-959, Rzeszów, POLAND; https://orcid.org/0000-0001-8795-2298

Olexandr Korchynskyi - Lab of Experimental Biology and Department of Biochemistry & General Chemistry, Faculty of Medicine, Rzeszów University, Warzywna 1a Str., 35-959, Rzeszów, POLAND; https://orcid.org/0000-0002-4557-4003

Ostap Kalyuzhnyi - Institute for Condensed Matter Physics of the National Academy of Sciences of Ukraine, 1 Svientsitskii str., 79011, Lviv, Ukraine; https://orcid.org/0000-0002-5691-3058

Dmytro Yaremchuk - Institute for Condensed Matter Physics of the National Academy of Sciences of Ukraine, 1 Svientsitskii str., 79011, Lviv, Ukraine; Institute of Applied Mathematics and Fundamental Sciences, Lviv Polytechnic National University, 12 S. Bandera Str., 79013, Lviv, Ukraine; https://orcid.org/0000-0003-2888-5878

Jaroslav Ilnytskyi - Institute for Condensed Matter Physics of the National Academy of Sciences of Ukraine, 1 Svientsitskii str., 79011, Lviv, Ukraine; Institute of Applied Mathematics and Fundamental Sciences, Lviv Polytechnic National University, 12 S. Bandera Str., 79013, Lviv, Ukraine; https://orcid.org/0000-0002-1868-5648

Taras Patsahan - Institute for Condensed Matter Physics of the National Academy of Sciences of Ukraine, 1 Svientsitskii str., 79011, Lviv, Ukraine; Institute of Applied Mathematics and Fundamental Sciences, Lviv Polytechnic National University, 12 S. Bandera Str., 79013, Lviv, Ukraine; https://orcid.org/0000-0002-7870-2219

Author Contributions

S.M. led the project, planned experiments, collected the data, and edited the manuscript. R.B. fabricated the surfaces, collected data, and co-wrote the manuscript. S.V.M. analyzed surfaces using AFM, conducted cell sorting image analysis, and co-wrote the manuscript. M.P. conducted cell culturing and cell sorting. R.M. and A.B. generated fluorescently labeled cell lines using lentiviral transduction. V.R. led experiments with cells. J.I. led the development of dissipative particle dynamics computing code for the thermosensitive and cross-linkable polymer films, coordinated simulations of the phase separation between PGMA and PNIPAM polymers, their crosslinking and pinning, and co-wrote a simulation part of a manuscript. OI.K. led the cell line generation, planned experiments, collected the data, and participated in the study's conceptualization and manuscript writing. T.P. developed a model and corresponding software for Monte Carlo simulations to study the adsorption and desorption of cells on a micropatterned surface, aimed at the theoretical prediction of cell sorting efficiency. Os.K. performed, analyzed, and visualized results for computer simulations for the phase separation between PGMA and PNIPAM polymers. D.Y. performed, analyzed, visualized, and wrote the part on computer

simulations for the effect of crosslinking of thermo-response of PNIPAM polymers and the effect of pinning of the PNIPAM gel onto the PGMA domains. M.P. and R.M. equally contributed to this work.

All the co-authors participated in editing the final version of the manuscript.

Notes

The authors declare no competing financial interest.

ACKNOWLEDGMENTS

The work was supported by the USA NSF Grant 2401713, (S.M., R.W.B., S.V.M., M.P.); National Scientific Centre (Poland) Grant 2023/05/Y/NZ3/00189 (OI.K., R.M. and A.B.) and STCU (Ukraine) Grant 7115. J.I., T.P., Os.K., and D.Y. acknowledge support by the project 7115 by U.S. National Academy of Sciences (NAS) and U.S. Office of Naval Research Global (ONRG). Computer time for reported simulations provided by the Interdisciplinary Center for Computer Simulations: creation, basic research, teaching and sustainability (supported by the NRFU grant no. 2023.05/0019).

REFERENCES

(1) Fulwyler, M. J. Electronic Separation of Biological Cells by Volume. *Science* **1965,** *150* (3698), 910-911.

(2) Plouffe, B. D.; Murthy, S. K.; Lewis, L. H. Fundamentals and Application of Magnetic Particles in Cell Isolation and Enrichment: A Review. *Rep. Prog. Phys.* **2015,** *78* (1), 1-38.

(3) Sutermaster, B. A.; Darling, E. M. Considerations for High-Yield, High-Throughput Cell Enrichment: Fluorescence Versus Magnetic Sorting. *Sci. Rep.* **2019,** *9* (1), 227.

(4) Qiu, X.; Lombardo, J. A.; Westerhof, T. M.; Pennell, M.; Ng, A.; Alshetaiwi, H.; Luna, B. M.; Nelson, E. L.; Kessenbrock, K.; Hui, E. E.; Haun, J. B. Microfluidic Filter Device with Nylon Mesh Membranes Efficiently Dissociates Cell Aggregates and Digested Tissue into Single Cells. *Lab on a Chip* **2018,** *18* (18), 2776-2786.

(5) Wu, Y.; Ren, Y.; Tao, Y.; Hou, L.; Jiang, H. High-Throughput Separation, Trapping, and Manipulation of Single Cells and Particles by Combined Dielectrophoresis at a Bipolar Electrode Array. *Anal. Chem.* **2018,** *90* (19), 11461-11469.

(6) Lu, H.; Gaudet, S.; Schmidt, M. A.; Jensen, K. F. A Microfabricated Device for Subcellular Organelle Sorting. *Anal. Chem.* **2004,** *76* (19), 5705-12.

(7) Du, M.; Kavanagh, D.; Kalia, N.; Zhang, Z. Characterising the Mechanical Properties of Haematopoietic and Mesenchymal Stem Cells Using Micromanipulation and Atomic Force Microscopy. *Med Eng Phys* **2019,** *73*, 18-29.
(8) Sims, N. R.; Anderson, M. F. Isolation of Mitochondria from Rat Brain Using Percoll Density Gradient Centrifugation. *Nat. Protoc.* **2008,** *3* (7), 1228-1239.
(9) Khare, P.; Pant, A. Cell Sorting: Underpinnings and Contemporary Developments. In *Flow Cytometry: Applications in Cellular and Molecular Toxicology*; Springer: 2025; pp 1-13.
(10) Gossett, D. R.; Weaver, W. M.; Mach, A. J.; Hur, S. C.; Tse, H. T. K.; Lee, W.; Amini, H.; Di Carlo, D. Label-Free Cell Separation and Sorting in Microfluidic Systems. *Anal. Bioanal.l Chem.* **2010,** *397* (8), 3249-3267.
(11) Shiri, F.; Feng, H.; Gale, B. K. Chapter 14 - Passive and Active Microfluidic Separation Methods. In *Particle Separation Techniques*; Contado, C., Ed.; Elsevier: 2022; pp 449-484.
(12) Du, Z.; Colls, N.; Cheng, K. H.; Vaughn, M. W.; Gollahon, L. Microfluidic-Based Diagnostics for Cervical Cancer Cells. *Biosens. Bioelectronics* **2006,** *21* (10), 1991-1995.
(13) Sin, A.; Murthy, S. K.; Revzin, A.; Tompkins, R. G.; Toner, M. Enrichment Using Antibody-Coated Microfluidic Chambers in Shear Flow: Model Mixtures of Human Lymphocytes. *Biotech. Bioeng.* **2005,** *91* (7), 816-826.
(14) Chang, W. C.; Lee, L. P.; Liepmann, D. Biomimetic Technique for Adhesion-Based Collection and Separation of Cells in a Microfluidic Channel. *Lab on a Chip* **2005,** *5* (1), 64-73.
(15) Bose, S.; Singh, R.; Hanewich-Hollatz, M.; Shen, C.; Lee, C.-H.; Dorfman, D. M.; Karp, J. M.; Karnik, R. Affinity Flow Fractionation of Cells Via Transient Interactions with Asymmetric Molecular Patterns. *Sci. Rep.* **2013,** *3* (1), 2329.
(16) Choi, S.; Karp, J. M.; Karnik, R. Cell Sorting by Deterministic Cell Rolling. *Lab on a Chip* **2012,** *12* (8), 1427-1430.
(17) Tasadduq, B.; McFarland, B.; Islam, M.; Alexeev, A.; Sarioglu, A. F.; Sulchek, T. Continuous Sorting of Cells Based on Differential P Selectin Glycoprotein Ligand Expression Using Molecular Adhesion. *Anal.l Chem.* **2017,** *89* (21), 11545-11551.
(18) Chrit, F. E.; Li, P.; Sulchek, T.; Alexeev, A. Adhesion-Based High-Throughput Label-Free Cell Sorting Using Ridged Microfluidic Channels. *Soft Matter* **2024,** *20* (8), 1913-1921.
(19) Kwon, K. W.; Choi, S. S.; Lee, S. H.; Kim, B.; Lee, S. N.; Park, M. C.; Kim, P.; Hwang, S. Y.; Suh, K. Y. Label-Free, Microfluidic Separation and Enrichment of Human Breast Cancer Cells by Adhesion Difference. *Lab on a Chip* **2007,** *7* (11), 1461-1468.
(20) Sniadecki, N. J.; Desai, R. A.; Ruiz, S. A.; Chen, C. S. Nanotechnology for Cell–Substrate Interactions. *Ann. Biomed.l Eng.* **2006,** *34* (1), 59-74.

(21) Lim, J. Y.; Hansen, J. C.; Siedlecki, C. A.; Runt, J.; Donahue, H. J. Human Foetal Osteoblastic Cell Response to Polymer-Demixed Nanotopographic Interfaces. *J. Royal Soc. Interface* **2005,** *2* (2), 97-108.
(22) Green, J. V.; Murthy, S. K. Microfluidic Enrichment of a Target Cell Type from a Heterogenous Suspension by Adhesion-Based Negative Selection. *Lab on a Chip* **2009,** *9* (15), 2245-2248.
(23) Housmans, C.; Sferrazza, M.; Napolitano, S. Kinetics of Irreversible Chain Adsorption. *Macromolecules* **2014,** *47* (10), 3390-3393.
(24) O'Shaughnessy, B.; Vavylonis, D. Irreversibility and Polymer Adsorption. *Phys. Rev. Lett.* **2003,** *90* (5), 056103-1 - 056103-4.
(25) Yu, C.; Granick, S. Revisiting Polymer Surface Diffusion in the Extreme Case of Strong Adsorption. *Langmuir* **2014,** *30* (48), 14538-14544.
(26) Aveyard, R.; Binks, B. P.; Clint, J. H. Emulsions Stabilised Solely by Colloidal Particles. *Adv. Colloid. Interface. Sci.* **2003,** *100*, 503-546.
(27) Nagrath, S.; Sequist, L. V.; Maheswaran, S.; Bell, D. W.; Irimia, D.; Ulkus, L.; Smith, M. R.; Kwak, E. L.; Digumarthy, S.; Muzikansky, A.; Ryan, P.; Balis, U. J.; Tompkins, R. G.; Haber, D. A.; Toner, M. Isolation of Rare Circulating Tumour Cells in Cancer Patients by Microchip Technology. *Nature* **2007,** *450* (7173), 1235-1239.
(28) Poulichet, V.; Garbin, V. Ultrafast Desorption of Colloidal Particles from Fluid Interfaces. *Proc. Natl. Acad. Sci. USA* **2015,** *112* (19), 5932-5937.
(29) Kurashina, Y.; Imashiro, C.; Hirano, M.; Kuribara, T.; Totani, K.; Ohnuma, K.; Friend, J.; Takemura, K. Enzyme-Free Release of Adhered Cells from Standard Culture Dishes Using Intermittent Ultrasonic Traveling Waves. *Commun. Biol.* **2019,** *2* (393), 1-11.
(30) Garcia, A. J.; Gallant, N. D. Stick and Grip: Measurement Systems and Quantitative Analyses of Integrin-Mediated Cell Adhesion Strength. *Cell Biochem. Biophys.* **2003,** *39*, 61-73.
(31) Murphy-Ullrich, J. E. The De-Adhesive Activity of Matricellular Proteins: Is Intermediate Cell Adhesion an Adaptive State? *J. Clinic.Investg.* **2001,** *107* (7), 785-790.
(32) Pierres, A.; Benoliel, A.-M.; Bongrand, P. Cell Fitting to Adhesive Surfaces: A Prerequisite to Firm Attachment and Subsequent Events. *Eur. Cell. Mater.* **2002,** *3*, 31-45.
(33) Anselme, K.; Ploux, L.; Ponche, A. Cell/Material Interfaces: Influence of Surface Chemistry and Surface Topography on Cell Adhesion. J. *Adhesion Sci. Techn.* **2010,** *24* (5), 831-852.
(34) Anselme, K.; Bigerelle, M.; Noel, B.; Dufresne, E.; Judas, D.; Iost, A.; Hardouin, P. Qualitative and Quantitative Study of Human Osteoblast Adhesion on Materials with Various Surface Roughnesses. *Journal of Biomedical Materials Research J. Biomed. Mater. Res. B Appl. Biomater.* **2000,** *49* (2), 155-166.

(35) Anselme, K.; Bigerelle, M. Modelling Approach in Cell/Material Interactions Studies. *Biomaterials* **2006,** *27* (8), 1187-1199.
(36) Kim, Y.; Laradji, A. M.; Sharma, S.; Zhang, W.; Yadavalli, N. S.; Xie, J.; Popik, V.; Minko, S. Refining of Particulates at Stimuli-Responsive Interfaces: Label-Free Sorting and Isolation. *Angew. Chem., Int. Edi.* **2022,** *61* (7), e202110990.
(37) Yamada, N.; Okano, T.; Sakai, H.; Karikusa, F.; Sawasaki, Y.; Sakurai, Y. Thermo-Responsive Polymeric Surfaces; Control of Attachment and Detachment of Cultured Cells. *Makromol. Chem, Rapid Commun.* **1990,** *11* (11), 571-576.
(38) Kim, Y.; Jahan, U.; Deltchev, A.; Lavrik, N.; Reukov, V.; Minko, S. Strategy to Non-Enzymatic Harvesting of Cells Via Decoupling of Adhesive and Disjoining Domains of Nanostructured Stimuli-Responsive Polymer Film. *ACS Appl. Mater. Interfaces* **2023**, *42* (15), 49012-49021.
(39) Badenhorst, R.; Makaev, S.; Yaremchuk, D.; Sajjan, Y.; Sulimov, A.; Reukov, V. V.; Lavrik, N. V.; Ilnytskyi, J.; Minko, S. Reversible Binding Interfaces Made of Microstructured Polymer Brushes. *Langmuir* **2024,** *40* (13), 7008-7020.
(40) Ilnytskyi, J.; Yaremchuk, D.; Minko, S. Interaction of Colloidal Particulates with Dynamic Microstructured Polymer Brushes: Computer Simulations. *Langmuir* **2025**, *41* (20), 12731-12744.
(41) Tsien, R. Y. The Green Fluorescent Protein. *Ann. Rev. Biochem.* **1998,** *67* (1), 509-544.
(42) Chalfie, M.; Tu, Y.; Euskirchen, G.; Ward, W. W.; Prasher, D. C. Green Fluorescent Protein as a Marker for Gene Expression. *Science* **1994,** *263* (5148), 802-805.
(43) Cabantous, S.; Terwilliger, T. C.; Waldo, G. S. Protein Tagging and Detection with Engineered Self-Assembling Fragments of Green Fluorescent Protein. *Nature biotechn.* **2005,** *23* (1), 102-107.
(44) Groot, R. D.; Warren, P. B. Dissipative Particle Dynamics: Bridging the Gap between Atomistic and Mesoscopic Simulation. *J. Chem. Phys.* **1997,** *107* (11), 4423-4435.

TOC image